

The 11th January 2018, Mw 6.0 Bago-Yoma, Myanmar earthquake: A shallow thrust event within the deforming Bago-Yoma Range

Wardah Fadir¹, Eric O. Lindsey¹, Yu Wang², Phyo Maung Maung³, Heng Luo⁴, Tint Lwin Swe⁵, Pa Pa Tun⁶, and Shengji Wei³

¹Nanyang Technological University

²National Taiwan University

³Earth Observatory of Singapore

⁴Wuhan University

⁵Myanmar Earthquake Committee

⁶Department of Meteorology & Hydrology, Myanmar

November 24, 2022

Abstract

On 11 January 2018 (18:26 UTC), a Mw 6.0 earthquake occurred approximately 30 km west of the Sagaing Fault in the Bago-Yoma Range (BYR). Using a local broadband seismic network and regional seismic stations, we refine the source parameters of the earthquake sequence. We relocate ~100 earthquake epicenters and determine the focal mechanism and centroid depth of the mainshock and 20 aftershocks with Mw>4. The relocated epicenters are distributed in an elongated zone oriented in a NW-SE direction that is consistent with the strike of the mainshock fault plane solution and the slip distribution derived from ALOS-2 InSAR observations. Most of the aftershocks have a pure thrust focal mechanism similar to the mainshock, except for four strike-slip aftershocks. The refined source parameters of the thrust events clearly delineate a fault dipping ~40° to the southwest at a depth range of 3-7 km, indicating that the earthquake sequence ruptured a previously unmapped, active fault. We interpret the earthquake sequence to be associated with pre-existing faults within the BYR anticlinorium. This earthquake sequence and historical seismicity indicate that the upper crust of the BYR is highly stressed, resulting in ongoing distributed deformation between the oblique Rakhine megathrust and the dextral Sagaing Fault. The seismic hazard posed by these active faults has been increasing with the development of infrastructure such as dams within the BYR. Our study highlights the need for high-resolution earthquake source parameter and strong ground motion attenuation studies for seismic hazard preparation and further understanding of the neotectonics of Myanmar.

1 **The 11th January 2018, Mw 6.0 Bago-Yoma, Myanmar earthquake: A shallow thrust**
2 **event within the deforming Bago-Yoma Range**

3
4 **Wardah Fadil^{1,2}, Eric O. Lindsey¹, Yu Wang³, Phyo Maung Maung¹, Heng Luo⁴, Tint Lwin**
5 **Swe⁵, Pa Pa Tun⁶, Shengji Wei^{1,2}**

6
7 ¹Earth Observatory of Singapore, Nanyang Technological University, Singapore

8 ²Asian School of the Environment, Nanyang Technological University, Singapore

9 ³National Taiwan University, Taiwan

10 ⁴State Key Laboratory of Information Engineering in Surveying, Mapping, and Remote Sensing,
11 Wuhan University, China

12 ⁵Myanmar Earthquake Committee, Myanmar

13 ⁶Department of Meteorology and Hydrology, Myanmar

14

15

16 Corresponding author: Shengji Wei (shjwei@ntu.edu.sg)

17 Wardah Fadil (wardahsh001@e.ntu.edu.sg)

18

19 **Key Points: (<140 characters)**

- 20
- 21 • We propose that the Mw6.0 Bago-Yoma earthquake ruptured a previously unmapped SW-dipping thrust fault at shallow depths within the Bago-Yoma Range anticlinorium.
 - 22 • The upper crust of the Burma plate between the megathrust and Sagaing Fault is
23 undergoing distributed deformation to partly accommodate the oblique convergence of
24 the Indian plate.
 - 25 • The proximity of mapped and potentially unidentified active faults within the Bago-
26 Yoma Range to dams and reservoirs indicate an increased seismic hazard.
- 27

28 Abstract (250 words)

29 On 11th January 2018 (18:26 UTC), a Mw 6.0 earthquake occurred approximately 30 km west of
30 the Sagaing Fault in the Bago-Yoma Range (BYR). Using a local broadband seismic network
31 and regional seismic stations, we refine the source parameters of the earthquake sequence. We
32 relocate ~100 earthquake epicenters and determine the focal mechanism and centroid depth of
33 the mainshock and 20 aftershocks with Mw>4. The relocated epicenters are distributed in an
34 elongated zone oriented in a NW-SE direction that is consistent with the strike of the mainshock
35 fault plane solution and the slip distribution derived from ALOS-2 InSAR observations. Most of
36 the aftershocks have a pure thrust focal mechanism similar to the mainshock, except for four
37 strike-slip aftershocks. The refined source parameters of the thrust events clearly delineate a fault
38 dipping ~40° to the southwest at a depth range of 3-7 km, indicating that the earthquake
39 sequence ruptured a previously unmapped, active fault. We interpret the earthquake sequence to
40 be associated with pre-existing faults within the BYR anticlinorium. This earthquake sequence
41 and historical seismicity indicate that the upper crust of the BYR is highly stressed, resulting in
42 ongoing distributed deformation between the oblique Rakhine megathrust and the dextral
43 Sagaing Fault. The seismic hazard posed by these active faults has been increasing with the
44 development of infrastructure such as dams within the BYR. Our study highlights the need for
45 high-resolution earthquake source parameter and strong ground motion attenuation studies for
46 seismic hazard preparation and further understanding of the neotectonics of Myanmar.

47

48 Plain Language Summary

49 Myanmar is known to host many earthquakes, where most of the large earthquakes in the past
50 have occurred along the strike-slip Sagaing Fault and along the interface of or within the Indian
51 plate that subducts beneath the Burma plate off the west coast of Myanmar. Less attention is
52 given to smaller magnitude and shallower earthquakes that occur in the region between the
53 subduction zone and the Sagaing Fault, due to lack of instrumentation to detect smaller
54 earthquakes and their less destructive potential. The 2018 Mw6.0 earthquake occurred in this
55 region within the Bago-Yoma Range (BYR) and was not associated with any mapped active
56 faults. We use seismological and geodetic data in addition to historical earthquake records and
57 existing geologic maps and surveys to study the earthquake. We propose that the earthquake
58 occurred on an existing shallow thrust fault within the BYR, which ruptured due to the region
59 accommodating part of the compression associated with the subduction, along multiple small-
60 scale crustal faults. We also highlight the increased seismic hazard in the region due to the close
61 proximity of these active faults to numerous dams.

62

63 1. Introduction

64 Myanmar is situated within a region of active tectonic blocks with boundaries defined by
65 a variety of tectonic settings (Fig. 1a). The Burma sliver plate is characterized by the highly
66 oblique convergence of the Indian plate (~18 mm/yr) at its western boundary while the ~N-S
67 striking right-lateral Sagaing Fault (~20 mm/yr) defines its eastern boundary bordering the Shan
68 Plateau on the Sunda plate (Socquet et al., 2006; Mallick et al., 2019). The Eastern Himalayan
69 Syntaxis represents the northern termination of the Burma plate while the Andaman Sea
70 spreading center separates the Burma sliver plate from the Sunda plate to the south. As a result,

71 the seismicity in Myanmar is highly active, with most of the historical seismicity distributed
72 along the plate-boundary-type Sagaing Fault, the Rakhine subduction zone, and within the
73 subducting Indian slab (Fig. 1b). Therefore, a majority of the seismological and geological
74 studies in the region have been focused on active structures associated with the subduction zone
75 and the Sagaing Fault (Le Dain et al., 1984; Ni et al., 1989; Chen & Molnar, 1990; Steckler et
76 al., 2008; Wang et al., 2013; Shyu et al., 2018).

77

78 While a significant amount of motion between the Indian and the Sunda Plate is
79 accommodated by the aforementioned plate boundary faults, recent studies show that shallow
80 earthquakes occur within the Central Myanmar Basin (CMB), indicating distributed deformation
81 within the Burma Plate (Chit Tet Mon et al., 2020). This distributed deformation may be
82 accommodated by numerous crustal faults, which are predominantly thrust faults close to the
83 eastern edge of the Western Range (WR; also known as Indo-Burma Range), as evidenced by
84 geological observations (e.g. Wang et al., 2014). Although accurate slip rates of these crustal
85 faults are still not available due to sparse GPS observations in southwest Myanmar, several
86 damaging shallow earthquakes have occurred such as the 2003 Mw 6.6 Taungdwingyi strike-slip
87 earthquake located ~48km to the west of the Sagaing Fault (Maung Thein et al., 2009), the 2007
88 Mw 5.6 NW-SE striking thrust earthquake (GCMT) on the western flank of the BYR, and two
89 damaging earthquakes in 1858 and 1927 (e.g., Oldham, 1883; Chibber, 1934; Le Dain et al.,
90 1984; Hurokawa & Maung Maung, 2011; Wang et al., 2014) (Fig. 1b). With recent rapid
91 economic growth and development of infrastructure (e.g. dams), the seismic hazard analysis in
92 SW Myanmar has become more pressing. The Mw 6.0 earthquake that occurred on 11th January
93 2018 (18:26 UTC) in the southern Bago-Yoma Range (BYR) raises the alarm to a higher level.

94

95 The BYR is a NNW-SSE trending uplifted region within the southeastern part of the
96 CMB with the major structural trend oriented sub-parallel to the Sagaing Fault (e.g., Bender,
97 1983). The highest elevation at its peak is ~550 m above sea level and is dwarfed in comparison
98 to the WR to the west and the Shan Plateau to the east. The northwestern and southern segments
99 of the BYR merge into the Salin and Prome subbasins, respectively (Pivnik et al., 1998). The
100 BYR has been interpreted as an anticlinorium within the larger synclinorium of the Central
101 Myanmar Basin, with outcrops exposing Miocene sandstones and shales (Naing Maw Than et
102 al., 2017). Geomorphic and geological studies show predominantly NNW-SSE and NW-SE
103 linear structures (Bender, 1983; Ridd & Racey, 2015; Sloan et al., 2017). Previous GPS studies
104 in Myanmar lack data within this area, thus, making seismic data one of the few resources
105 currently available to understand the ongoing deformation within the BYR.

106

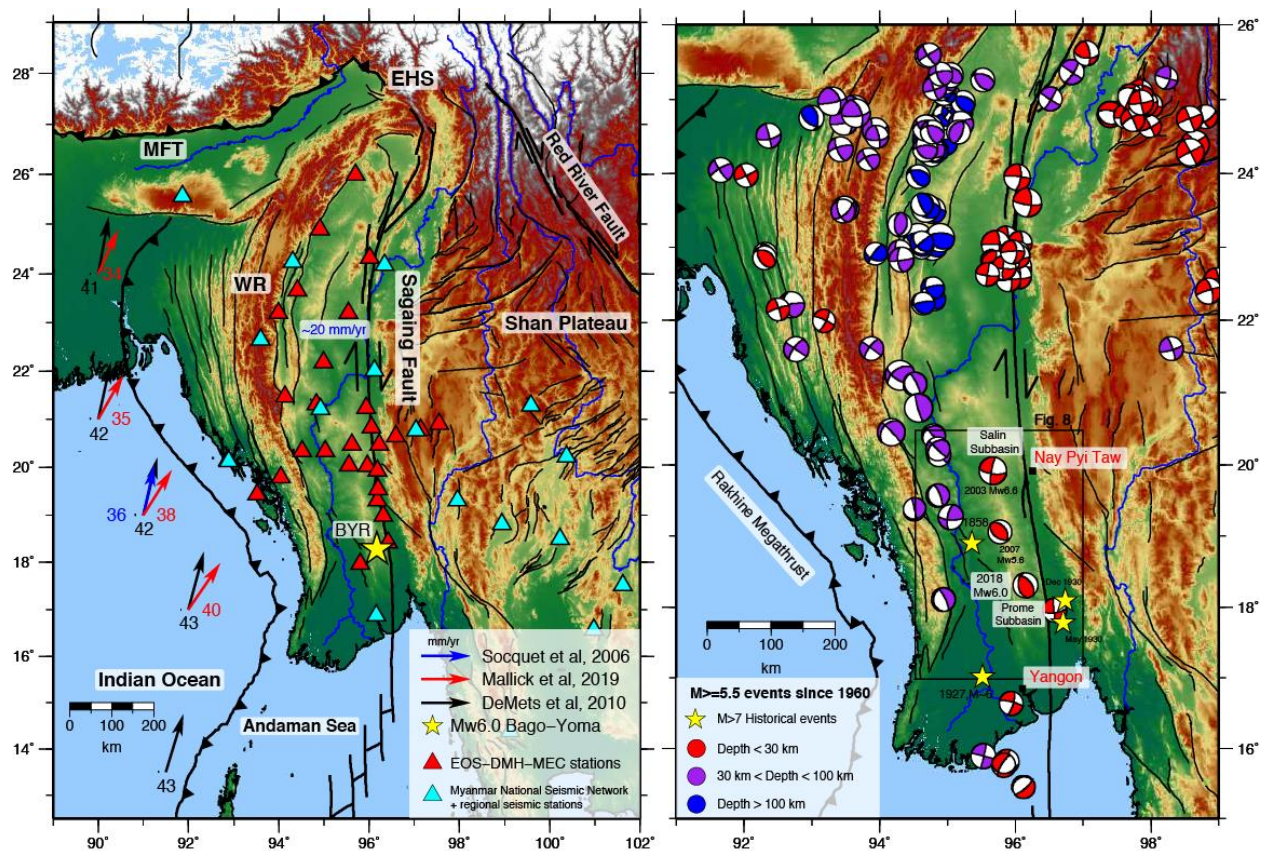
107 Early reports (e.g. NEIC, GCMT, GFZ) of the 2018 mainshock indicate a source depth
108 ranging from 9-12 km and a thrust focal mechanism on a 40°- 50° dipping fault plane striking
109 NNW-SSE, with 30 $M > 4$ aftershocks as reported by NEIC. Yet, such a thrust fault at the
110 mountainous epicenter region of the earthquake has not been mapped as an active fault, due to
111 limited geological and geophysical observations. This earthquake sequence was well recorded by
112 a broadband seismic network that was recently installed by the collaboration between EOS-
113 DMH-MEC (Earth Observatory of Singapore – Department of Meteorology and Hydrology,
114 Myanmar – Myanmar Earthquake Committee) and the Myanmar national broadband seismic

115 network (Hrin Nei Thiam et al., 2017) (Fig. 1a). It provides a unique dataset for us to better
 116 constrain the source parameters of the earthquakes and therefore, better understand their tectonic
 117 implication, as well as the seismic hazards from such crustal faults.

118

119 In this study, we first use the P-wave arrival time recorded by the regional broadband
 120 network to relocate the epicenter of the earthquake sequence. We then apply a waveform
 121 inversion method to precisely determine the focal mechanism and centroid depth of the
 122 mainshock and 20 $M > 4$ aftershocks that occurred between January – June 2018. The seismicity
 123 and fault geometry are then verified by a slip model derived from InSAR ALOS-2 data. This is
 124 followed by a discussion on the seismotectonic implications of our findings and the seismic
 125 hazard that this newly identified fault and other potential unidentified active faults pose due to
 126 their assumed inactivity and proximity to the dams and reservoirs.

127



128

129 **Figure 1. Regional tectonics and historical seismicity in Myanmar.** (Left) Location of seismic
 130 stations in Myanmar used in this study. Arrows indicate motion of the Indian plate relative to the
 131 Shan Block/Plateau (red) and motion of the Indian plate relative to the Sunda plate (blue, black).
 132 Regional faults modified from Wang et al. (2014) and Taylor & Yin (2009) (black lines). (Right)
 133 Focal mechanisms of historical earthquakes ($M > 5.5$) from global earthquake catalogs
 134 (Dziewonski et al., 1981; Ekstrom et al., 2012). Location of $M > 7$ historical earthquakes (yellow
 135 stars) were obtained from Le Dain et al. (1984), Hurukawa & Maung Maung (2011) and Wang et
 136 al. (2014). MFT – Main Frontal Thrust, EHS – Eastern Himalayan Syntaxis, WR – Western
 137 Range, BYR – Bago-Yoma Range.

138 **2. Data and Methods**

139 2.1 Earthquake epicenter relocation and focal mechanism inversion

140 The Mw 6.0 mainshock occurred in the southern part of the BYR, ~30 km west of
 141 the Sagaing Fault and ~35 km southwest of Phyu city. Approximately 100 $M_L > 1.5$
 142 aftershocks were reported by the EOS-DMH-MEC seismic network. The earthquake
 143 sequence was well-recorded by the seismic network and at least 4 stations (M011, M012,
 144 M003, M004) recorded the mainshock and aftershocks within a distance of <100 km,
 145 allowing the P-wave arrival of aftershocks with $M > 1.5$ to be well-identified at these
 146 stations. We tested various 1D velocity models extracted from CRUST1.0 (Laske et al.,
 147 2013) in both travel-time and waveform analysis and found that the model at (18.5°N,
 148 96.5°E) (Fig. S1) performs the best. With this model, we relocated the epicenter of the
 149 mainshock and aftershocks using a grid-search technique. Assuming a source depth of 7
 150 km, we searched for the best epicenter and origin time (t_0) for each event by minimizing
 151 the residual travel time between the data (T_{obs}) and the calculated P-wave travel time
 152 (T_{calc}) at each station i for $N=4$ closest stations:

153

$$Error = \frac{1}{N} \sum_{i=1}^N (T_{obs_i} - T_{calc_i} - t_0)^2$$

154

155 To further refine the location of similar events within a cluster, we modified the
 156 method to locate events relative to a reference event. This is achieved by extracting
 157 station correction values to the P-wave travel time for the best earthquake location in the
 158 initial grid search and applying those values to the subsequent grid search relocation.

159 To determine the focal mechanism of the earthquakes, we adopted the
 160 generalized Cut-And-Paste (gCAP) waveform inversion method (Zhu & Helmberger,
 161 1996; Zhu and Ben-Zion, 2013), which cuts the three-component (R,T,Z) waveforms into
 162 Pnl and Surface wave segments and fits them with synthetics from a given velocity model
 163 while allowing different time shifts for each segment. The inversion searches through the
 164 best combination of strike, dip and rake values to produce synthetics that minimize the
 165 error function and the inversion is repeated at a range of depth values to determine the
 166 best centroid depth. The synthetics were derived from a Green's function library
 167 calculated at a range of depths and epicentral distances from the earthquake source using
 168 the frequency-wavenumber integration method (Zhu & Rivera, 2002) and the same 1D
 169 CRUST1.0 velocity model used in the travel-time analysis. Routine waveform data
 170 processing was conducted prior to the analysis which include removal of instrument
 171 response and rotation of horizontal components to radial and tangential components.

172 For the Mw 6.0 mainshock, waveforms from nearly all EOS-DMH-MEC and
 173 Myanmar National Seismic Network broadband stations in Myanmar were used. To
 174 improve the azimuthal coverage, broadband stations in Thailand were also included

175 (CHTO, CMMT, CRAI). For the $M > 4$ aftershocks, we included as many regional stations
176 as possible with good signal-to-noise ratio in the inversion. The inversion was conducted
177 at a frequency range of 0.02 – 0.08 Hz for the Pnl segments and 0.02 – 0.06 Hz for the
178 surface wave segments. We removed waveform segments that were clipped and excluded
179 complicated waveforms at stations close to the coast and located on thick sediments. The
180 inversion was repeated at 1 km intervals for a shallow depth range of 1-20 km.

181 Depth is a critical source parameter to define the fault geometry with seismicity.
182 To verify the centroid depths obtained from the gCAP inversions, we further inspected
183 the amplitude ratios between the Pnl waves and surface waves. The surface-/Pnl-wave
184 amplitude ratio for earthquakes recorded at a nearby station should decrease as the depth
185 of the earthquake increases, assuming the radiation pattern of the earthquakes are similar.
186 We selected a subset of similar thrust-faulting aftershocks that are located within 2 km of
187 the AA' profile, which is perpendicular to the strike of the fault. We plotted the surface-
188 /Pnl-wave amplitude ratio of these events as a function of distance from station M011
189 (Fig. 5a). The depth phases of these events at the M011 station were also examined to
190 verify the depths (Fig. 5b).

191

192 2.2 InSAR observation and inversion

193 To determine the surface deformation caused by the earthquake, we processed L-
194 band interferometric synthetic aperture radar (InSAR) data collected by the ALOS-2
195 satellite operated by the Japanese Aerospace Agency (JAXA). The L-band data collected
196 by this satellite works well in densely vegetated or forested areas such as the BYR; we
197 also processed C-band data collected by the European Space Agency's Sentinel-1
198 satellite but found that it did not maintain sufficient interferometric coherence to map the
199 deformation. We used the ALOS-2 wide-swath interferometric pair collected on
200 2017/12/26 and 2018/3/06 along descending Path 41, Frame 3250. We processed the data
201 using GMTSAR software (Sandwell et al., 2011), with topographic corrections from the
202 Shuttle Radar Topography Mission Global 1 arc second dataset (SRTMGL1; NASA JPL
203 2013), and unwrapped the phase using Snaphu (Chen & Zebker, 2000). We removed long
204 wavelength artifacts from the interferogram using a highpass gaussian filter with a
205 wavelength of 100 km and removed topographically-correlated atmospheric noise using a
206 simple linear regression. To reduce the high-resolution image to a more feasible number
207 of observation points for modeling, we downsampled the data using a variance-based
208 quadtree algorithm (Simons et al., 2002) with a variance threshold of 12 mm. The
209 original and detrended interferograms and the final set of resampled points are shown in
210 Fig. S2. We then applied an inversion algorithm proposed by (Jónsson et al., 2002) to the
211 downsampled data to determine the static slip distribution on the fault. The same 1D
212 velocity model as used in the waveform inversion was used to compute the static Green's
213 function library. We attempted the inversion on both possible fault planes.

214

215 3. Results

216

3.1 Epicenter relocation and focal mechanism inversion

217

218

219

220

221

222

223

224

225

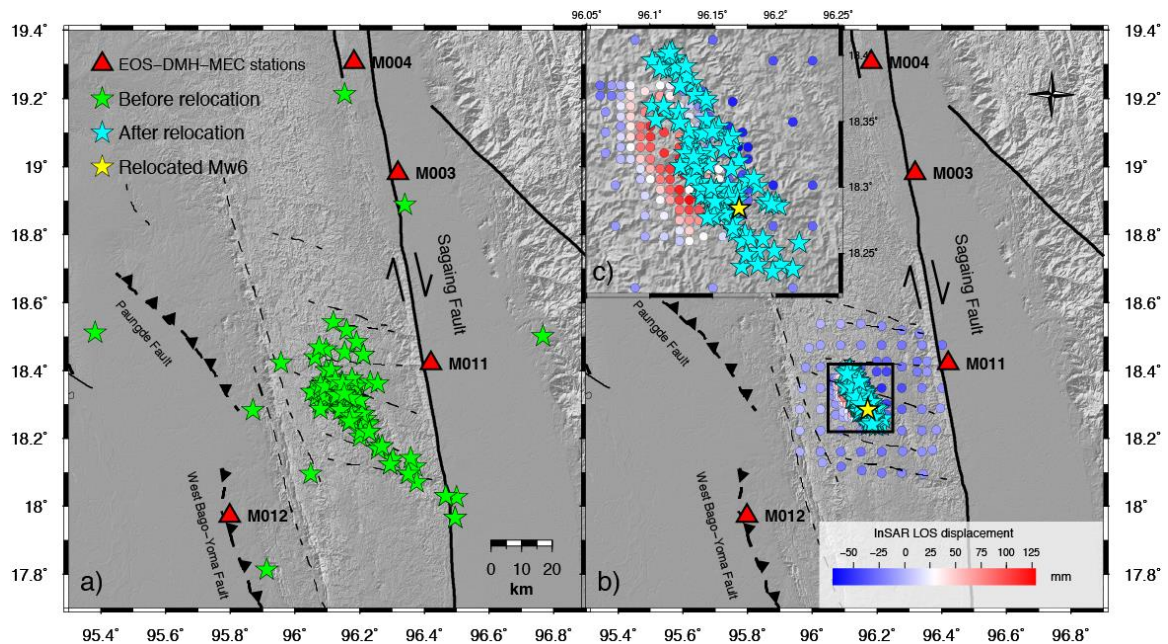
226

227

228

229

The epicenter relocation results in an elongated cluster of earthquakes striking NW-SE with dimensions of ~20km long and ~8 km wide, located in between the strike-slip Sagaing Fault to the east and the reverse Paungde Fault and West Bago Yoma Fault to the west (Fig. 2). The epicenter relocations converge into a tighter cluster compared to their initial locations. The relative horizontal location uncertainty is as small as ~1km, given the close proximity of the seismic stations (<100km) (Fig. S3). Observations of ground displacement from InSAR data (ALOS-2, descending) show that the epicenter relocations overlap with the area of maximum ground displacement, which also has an elongated NNW-SSE striking orientation, thus validating the accuracy of our epicenter relocations (Fig. 2c). The lack of a post-earthquake field survey means we cannot confirm whether the fault ruptured to the surface or not, however, the gradual shifts in the deformation pattern of the InSAR data (Fig S2) indicate that the rupture did not reach to the surface. This is later verified by the static slip inversions.



230

231

232

233

234

235

236

237

238

Figure 2. Earthquake relocation results using grid-search technique. (a) Initial epicenters of mainshock and ~100 aftershocks. Red triangles represent location of the four closest seismic stations used in the relocation process. (b) Relocated epicenters clustered in a NW-SE elongated trend within the BYR, consistent with the observed pattern of maximum ground displacement indicated by InSAR ALOS-2 ground displacement (colored circles). (c) Zoomed in plot of the black square rectangle, showing the distribution of epicenters and InSAR ground displacement. Solid and dashed black lines are active and inferred faults from Bender, 1983 and Wang et al., 2014.

239

240

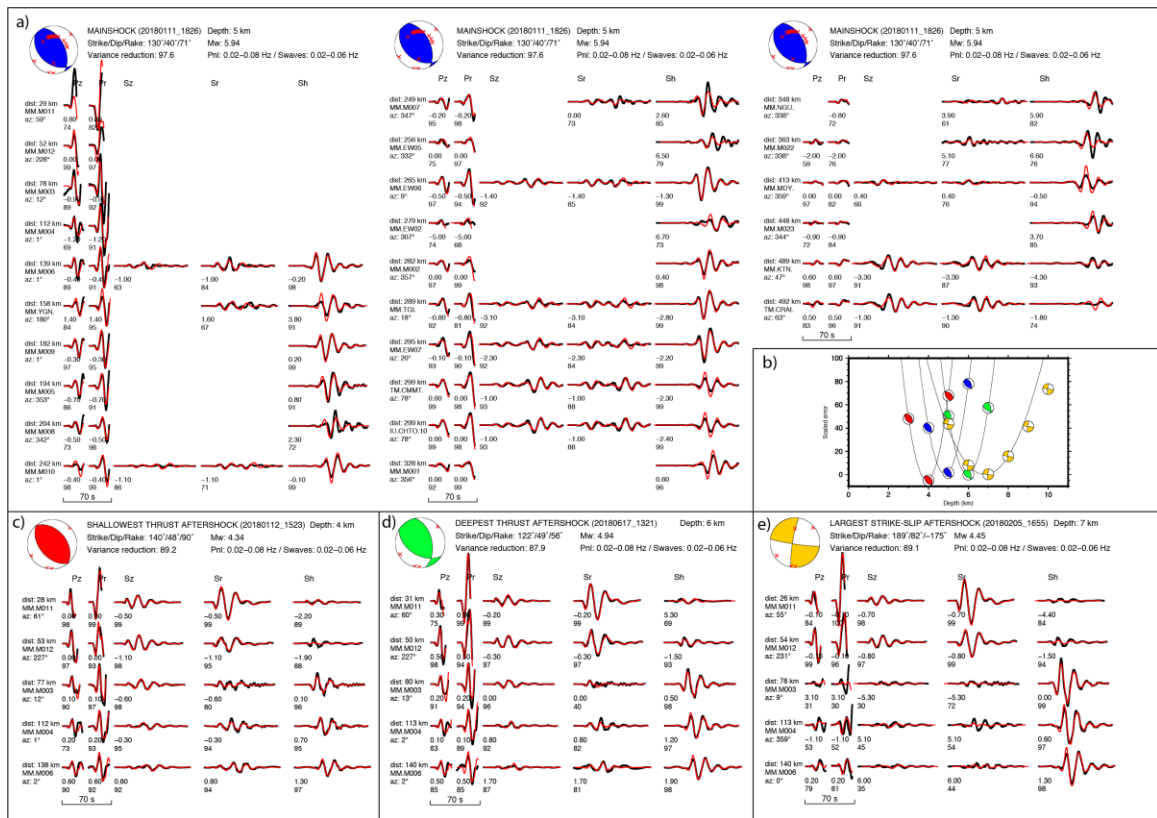
241

The waveform inversion for the Mw 6.0 mainshock results in a thrust-faulting focal mechanism (strike=130°/334°, dip=40°/53°, rake=71°/105°), in which the strike

242 values are consistent with NW-SE strike of the fault inferred from epicenter relocation
243 and InSAR observations (Fig 3a and 4) . The surface wave segments for the four closest
244 stations (M011, M012, M003, M004) are excluded from the inversion due to the
245 waveforms being clipped. The grid search results for the depth indicate that the
246 mainshock occurred at a shallow depth of 4.8 km (Fig. 3b). At the selected frequency
247 range (see Fig. 3), the inversion results in good waveform fits between data and
248 synthetics for stations <500 km from the epicenter. However, waveform segments from
249 several stations are too complicated to be well-fit by the 1D velocity model and are tuned
250 off in the inversion. These stations are either located near the coastline or within the
251 central Myanmar basin on top of thick layers (up to 18 km) of sediment (Pivnik et al.,
252 1998). The depth search result is shown as a plot of normalized error values as a function
253 of depth and is well-resolved at this frequency range, which shows a sharp convergence
254 at the best depth (Fig. 3b).

255 The inversion of 16 aftershocks with $M > 4$ located within 6 km of the mainshock
256 also show similar thrust-faulting mechanisms as the mainshock with depths ranging from
257 3-7 km. The shallowest thrust-faulting aftershock has a similar focal mechanism as the
258 mainshock (strike= $140^{\circ}/320^{\circ}$, dip= $48^{\circ}/42^{\circ}$, rake= $90^{\circ}/90^{\circ}$) and is located about 1 km
259 northeast of the mainshock at a depth of 3.9 km (Fig 3b, c). The deepest thrust-faulting
260 aftershock (strike= $122^{\circ}/347^{\circ}$, dip= $48^{\circ}/52^{\circ}$, rake= $56^{\circ}/55^{\circ}$) is located at about 2 km
261 southwest of the mainshock at a depth of 6 km (Fig. 3b, d). The waveform fits for these
262 events are also good for stations <500 km away and the depths are well-resolved (also see
263 Fig. S4). We observe that the ratio between the Pnl and surface wave segments of station
264 M011 are larger for the shallower aftershock than the deeper aftershock (Fig. 3c,d). We
265 also note that at these selected stations, the amplitude ratios between Sv and Sh waves are
266 different between the two events. Excellent fits between the synthetics and observations
267 provide strong constraints to both the focal mechanism and depth

268 Interestingly, the inversions show that four aftershocks are strike-slip events.
269 Three of these strike-slip events occur as a cluster at slightly larger depths (7-8 km) than
270 the thrust events, located at about 2 km to the east of the mainshock epicenter.
271 Approximately one month after the mainshock another strike-slip aftershock occurred at
272 ~6 km to the northwest of the mainshock epicenter. The largest ($M_w 4.5$) strike-slip event
273 has an almost pure strike-slip focal mechanism (strike= $189^{\circ}/98^{\circ}$, dip= $82^{\circ}/85^{\circ}$, rake=
274 $-175^{\circ}/-8^{\circ}$) and is located at a depth of 6.8 km (Fig 3b, e). The amplitude ratio between the
275 tangential component and Pnl component is clearly larger for these strike-slip events
276 compared with the thrust events, despite their depth being a few km larger. Although the
277 waveform fits to a few Pnl wave segments (e.g. M003) for the strike-slip events are
278 slightly worse than that for the thrust events, the fits to the other components are quite
279 decent to conclude that a cluster of strike-slip aftershocks occurred to the east of the
280 mainshock at deeper depths than the thrust events. Complete waveform fit results for all
281 stations and depth inversion plots are shown in Fig. S4a-d.



282

283

284

285

286

287

288

289

290

291

292

293

294

295

296

297

298

299

300

301

Figure 3. Cut-And-Paste inversion results. (Top panel) (a) Waveform fits between synthetics (red) from best the focal mechanism and the observed waveform (black) for the Mw6.0 mainshock. The best focal mechanism is shown in the top left. Station name is indicated at the leftmost column, along with its distance and azimuth from the epicenter. The waveform segments from left to right are as follows: Pnl – Z component, Pnl – Radial component, S-waves – Z component, S-waves – Radial component, S-waves – Tangential component. The first number below each waveform segment indicates the time shift (sec) followed by the waveform cross-correlation coefficient (%). (b) Plot of errors for various depth normalized to the minimum error, showing the best depth for the mainshock at ~4.8km. (Bottom panel) CAP inversion results for the shallowest (3.9 km) thrust aftershock (c), deepest (6.0km) thrust aftershock (d) and largest strike slip aftershock (e).

With the refined earthquake locations and source parameters, we can clearly see a lineation of the thrust events along a fault that dips $\sim 40^\circ$ in the depth profile (A-A') (Fig. 4), which is highly consistent with our point source focal mechanism solution for the Mw 6.0 mainshock. This seismicity profile suggests that the mainshock ruptured a SW-dipping fault. A list of the inverted source parameters for the mainshock and aftershocks is shown in Table 1.

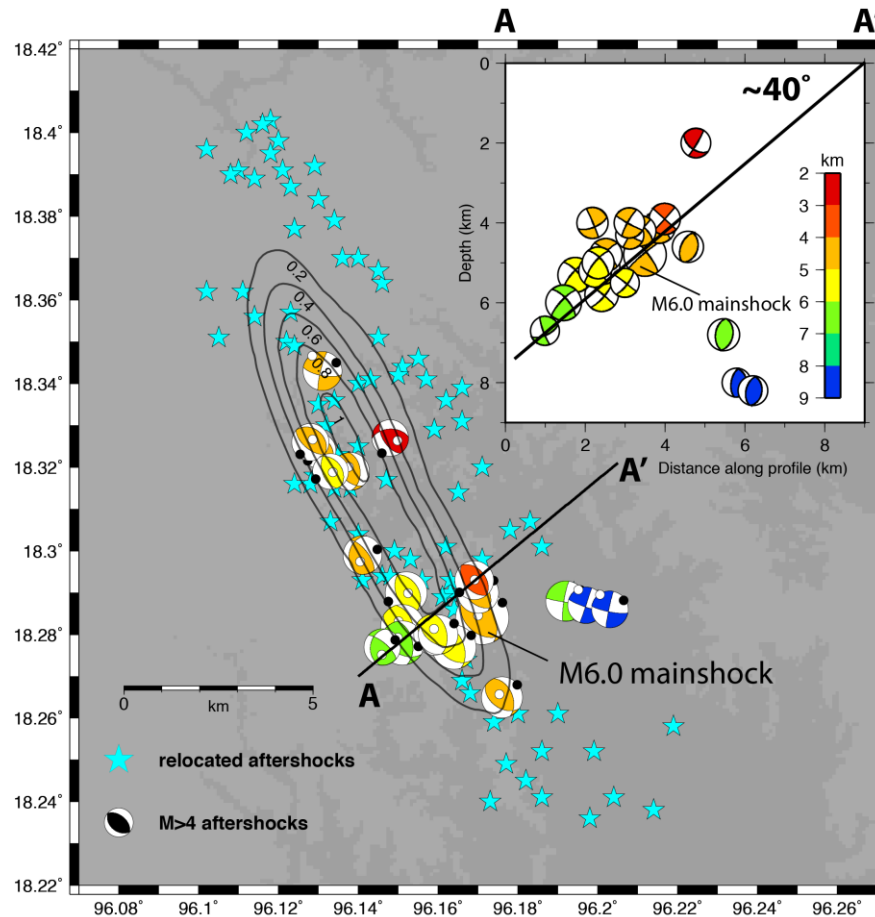
302

303

Table 1: Focal mechanisms, centroid depth, moment magnitude of mainshock and 20 $M > 4$ aftershocks from CAP inversion.

No.	Date	Time (UTC)	Lon	Lat	Nodal Plane 1 (Strike/Dip/Rake)	Nodal Plane 2 (Strike/Dip/Rake)	Depth (km)	Mw
1.	2018/01/11	18:26:24	96.171	18.284	130/40/71	334/53/105	4.8	5.94
2.	2018/01/11	20:08:41	96.148	18.327	268/50/43	147/59/131	2.0	4.09
3.	2018/01/12	15:23:55	96.169	18.293	140/48/90	320/42/90	3.9	4.34
4.	2018/01/12	04:16:03	96.128	18.326	130/61/90	310/29/90	4.0	4.19
5.	2018/01/13	23:29:47	96.138	18.319	139/50/64	356/46/118	4.2	4.20
6.	2018/01/13	13:51:15	96.130	18.324	310/29/82	139/61/94	4.3	3.93
7.	2018/01/14	17:49:56	96.131	18.343	101/71/-8	194/82/-161	4.6	4.35
8.	2018/01/17	07:43:27	96.133	18.319	323/37/77	159/54/100	5.5	4.01
9.	2018/01/22	07:37:59	96.141	18.299	322/67/67	189/32/133	4.0	4.31
10.	2018/02/05	16:55:35	96.192	18.288	189/82/-175	98/85/-8	6.8	4.45
11.	2018/02/07	16:38:01	96.203	18.286	101/79/-4	192/86/-169	8.2	4.10
12.	2018/02/09	18:04:25	96.197	18.287	109/82/1	19/89/172	8.0	4.03
13.	2018/03/04	10:48:10	96.176	18.265	336/48/112	125/46/67	4.8	4.54
14.	2018/03/17	19:59:04	96.152	18.290	328/40/82	158/50/97	5.8	4.63
15.	2018/04/20	22:29:24	96.164	18.277	128/42/64	341/53/112	5.1	4.87
16.	2018/04/20	04:16:02	96.159	18.280	121/51/59	345/48/122	5.2	4.53
17.	2018/04/21	22:41:11	96.160	18.280	119/50/51	351/54/127	5.0	4.40
18.	2018/04/22	18:31:44	96.170	18.290	330/47/100	136/44/80	4.1	4.53
19.	2018/04/24	12:23:34	96.151	18.282	120/50/59	343/49/122	5.3	4.82
20.	2018/06/17	13:21:31	96.151	18.278	122/49/56	348/51/123	6.0	4.94
21.	2018/06/17	13:42:35	96.146	18.277	310/70/61	188/35/143	6.7	4.04

304



305

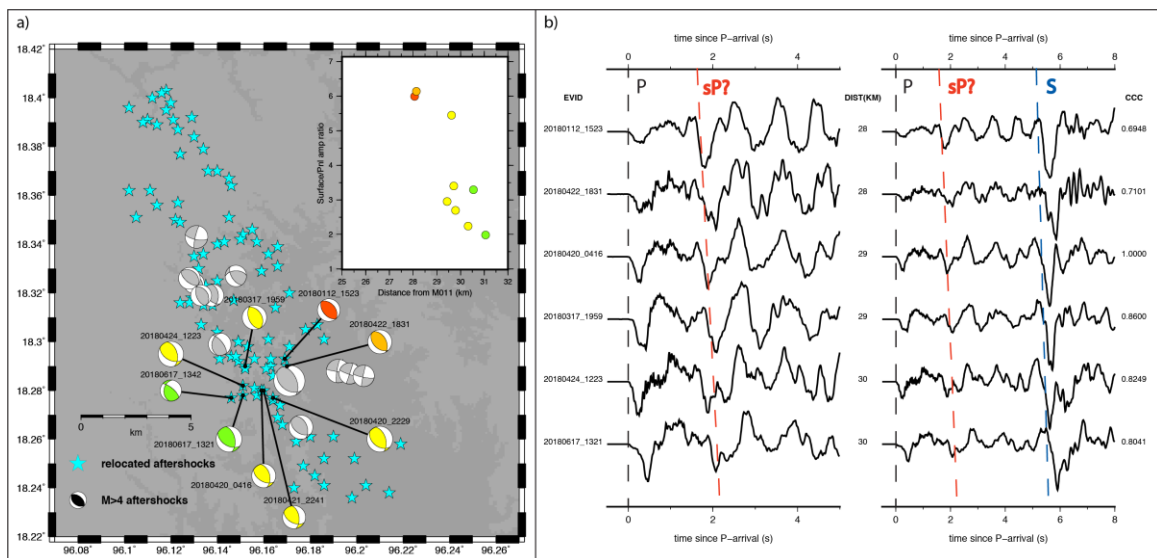
306 **Figure 4. Relocated epicenters of mainshock and ~100 aftershocks and focal**
 307 **mechanisms of 20 M>4 aftershocks.** Focal mechanisms are colored by depth. Black
 308 circles represent P-axis and white circles represent T-axis. Black contours represent
 309 coseismic slip derived from static slip inversion. (Inset) Cross-section plot along A-A',
 310 indicating a thrust fault dipping $\sim 40^\circ$ to the southwest rupturing at a depth range of (~ 3 - 6
 311 km) and a strike-slip fault rupturing at a deeper depth of (~ 7 - 8 km).

312

313 3.2 Surface-/Pnl- wave amplitude ratio and depth phase analysis

314 To further validate our depth inversion results and the inferred fault geometry, we
 315 look at the surface-/Pnl-wave amplitude ratios and the possible depth phases of nine
 316 thrust-faulting aftershocks along the profile A-A'. The plot of surface-/Pnl-wave
 317 amplitude ratio as a function of distance from station M011 for these aftershocks show
 318 that despite their slightly smaller distances, the shallower events indeed have larger
 319 amplitude ratios (inset in Fig 5a). This supports our depth inversion results, since
 320 shallower events generate larger amplitude surface waves relative to the body waves.

321 We also produced record-sections of six thrust aftershocks at the closest station
 322 (M011, 28-30 km away from the events) (Fig 5, right panel). The waveforms for each
 323 event are aligned at the P-wave arrivals and sorted by distance from the station (closer
 324 events are shallower). Although it is difficult to model these broadband waveforms with a
 325 1D velocity model, we can still identify the second largest peak after the P-arrival (~2
 326 seconds after) as a possible depth phase (sP) and observe its moveout in the record
 327 section. The event with the shallowest depth (20180112_1523: 3.9 km), which is closest
 328 to the station, has the earliest depth phase arrival, while the deepest event
 329 (20180617_1321: 6 km), which is the furthest from station M011, has the latest depth
 330 phase arrival. This moveout is consistent with the depth variation we obtained from the
 331 focal mechanism inversion. The arrivals of the S-wave relative to P-wave also increase as
 332 a function of distance. Even though the observed moveouts occur over a duration of less
 333 than one second and requires careful picking of the P-wave arrival, it is consistent with
 334 the spatial distribution of the events that span a horizontal distance range of ~3 km and a
 335 vertical distance range of ~2km.



336

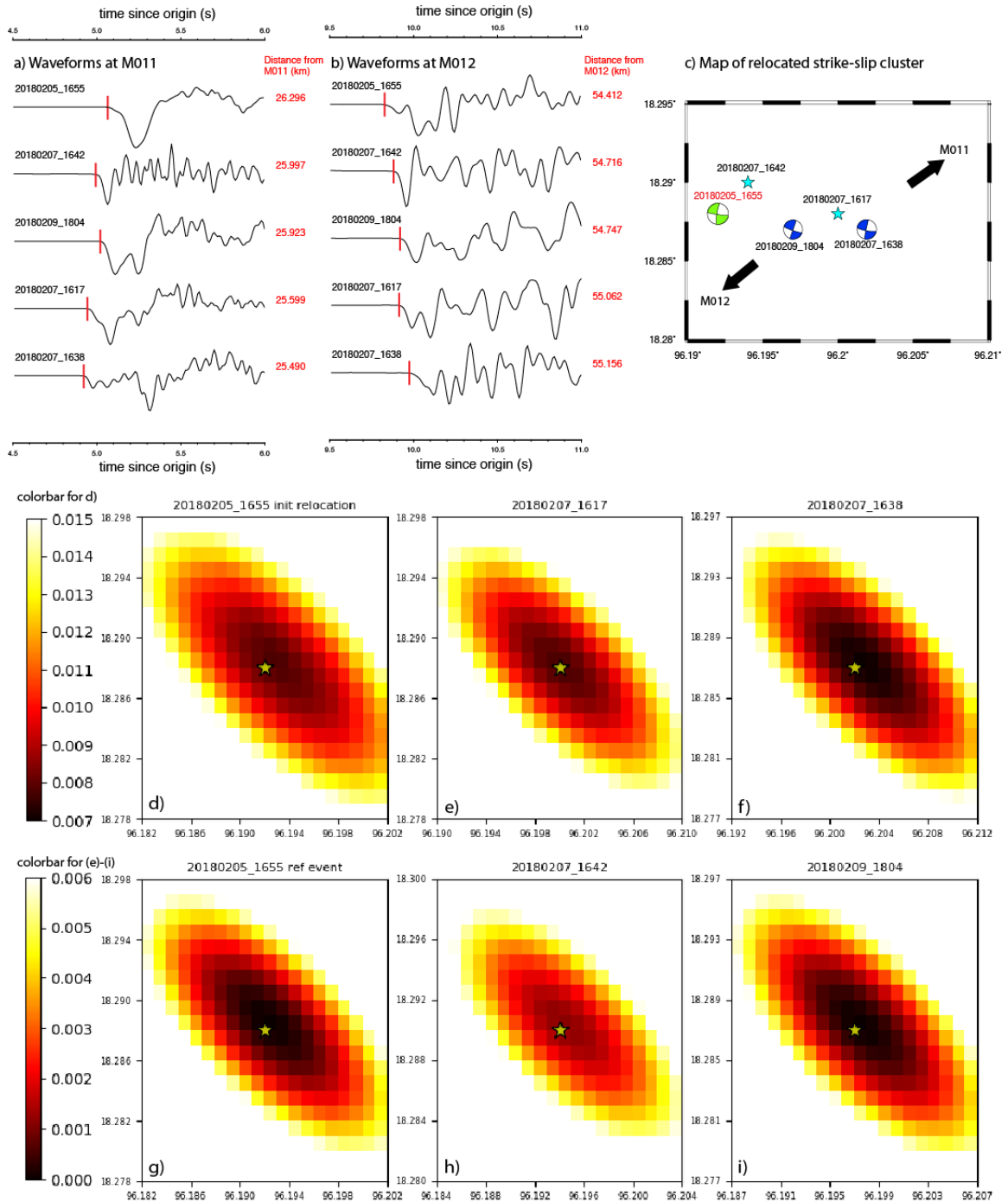
337 **Figure 5. Depth analysis of M>4 thrust aftershocks.** (a) Plot of focal mechanisms
 338 similar to Fig. 4 but with earthquakes included in the depth analysis indicated by focal
 339 mechanisms colored by depth. (Inset) Plot of Surface-/Pnl-wave amplitude ratio against
 340 the distance from the nearest station M011 for the selected focal mechanisms, showing a
 341 decreasing Surface-/Pnl amplitude ratio with increasing distance from M011, indicating a
 342 deeper source depth with increasing distance from the station. (b) Waveforms of the
 343 selected aftershocks aligned by the P-arrival time. The event name, distance from station
 344 M011 and cross-correlation coefficient of each waveform with event 20180420_0416 are
 345 indicated. The high cross-correlation coefficient values support the similarity of the
 346 epicenter and source mechanism of each thrust aftershock. The potential depth phase (sP)
 347 is indicated and shows a moveout with increasing distance from station M011, supporting
 348 a deeper source depth with increasing distance from the station.

349

350 3.3 Relative relocation of strike-slip earthquake cluster

351 Located at ~2km to the east of the mainshock epicenter, three of the four events
352 with strike-slip focal mechanism form a sub-cluster of the seismicity. To determine
353 which nodal plane is the ruptured fault, we further refined the location of the aftershocks
354 within this sub-cluster relative to the location of the largest strike-slip aftershock
355 (20180205_1655) (Fig. 6). The relative P-wave arrival times at station M011 and M012
356 between all five events in this cluster directly shows the sensitivity to the event location
357 (Fig. 6a-c), where the event nearest to station M011 (20180207_1638) has the earliest P-
358 arrival while the event furthest from M011 (20180205_1655) has the latest P-arrival and
359 vice versa at station M012. The largest axis of the error ellipse in the grid search results
360 indicates that the location uncertainty is well-constrained to within 1km (Fig 6d-i). These
361 three events align nicely along the strike (98°) of one of the fault plane solutions (Fig. 4e,
362 Table 1), indicating that the near E-W oriented strike-slip fault had ruptured during the
363 sequence, which is almost perpendicular to the active faults that were recently found in
364 northern Myanmar (Chit Tet Mon et al., 2020). The northernmost strike-slip event
365 suggests that the rupture happened on another strike-slip fault that is probably parallel to
366 the fault defined by the other three strike-slip event. Note that these strike-slip faults are
367 almost perpendicular to the Sagaing Fault.

368



369

370

371

372

373

374

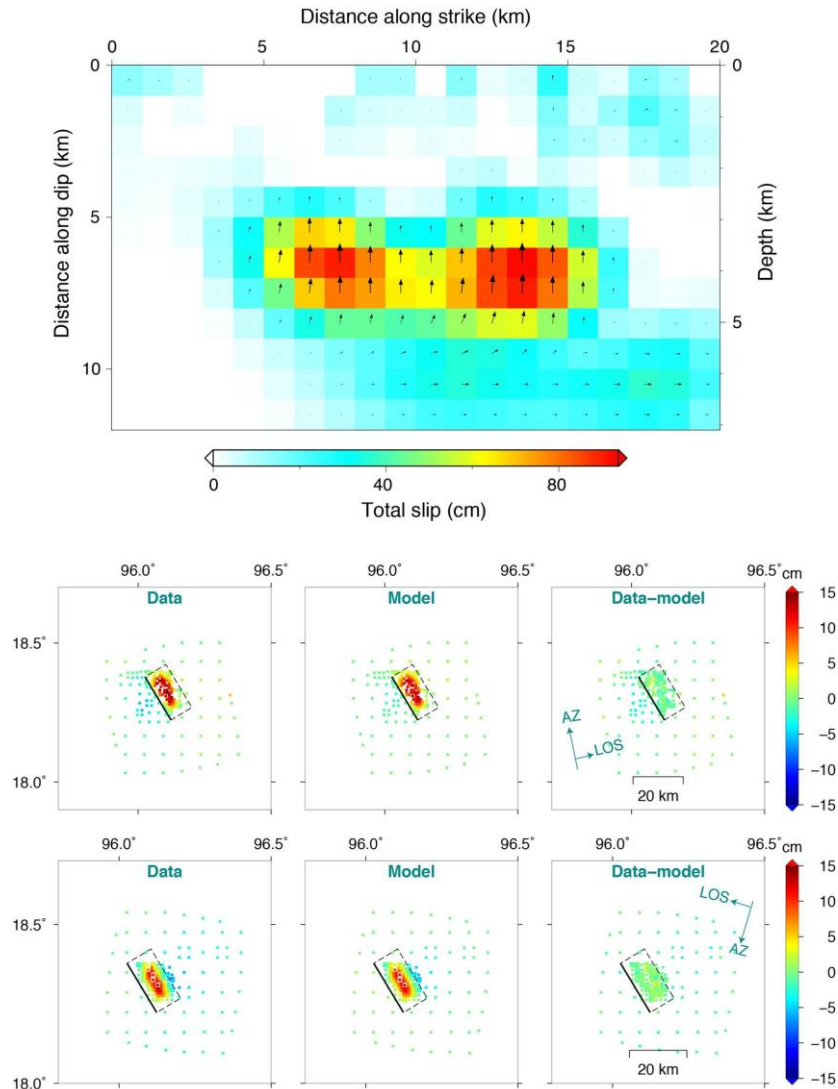
Figure 6. Strike-slip cluster indicate mainshock triggered an ~E-W trending left-lateral fault to the east of the mainshock epicenter. (a-b) Waveforms of the 5 events in the cluster at station M011 and M012, showing the increasing P-wave arrival time (red line) with increasing distance from each station. (c) Location of relocated aftershocks

375 relative to the reference event (20180205_1655). (d) L2-error plot for the initial grid
376 search relocation of the reference event. (e-i) L2-error plot for events in the cluster after
377 applying station correction values to the grid search.

378

379 3.4 Static slip inversion

380 The static slip models derived from both ascending and descending InSAR data
381 for two possible fault planes are presented in Fig. 7 (southwest-dipping fault) and Fig S5
382 (northeast dipping fault). The inversion results show that both fault planes can fit the data
383 almost equally well. Although the northeast dipping fault can fit the data slightly better,
384 the difference in misfit is so small (1.68 cm vs 1.50 cm) that it could be ignored
385 considering the other uncertainties (e.g. 3D structure). The southwest dipping fault plane
386 inversion prefers a fault geometry that strikes 157° and dips 49° , highly consistent with
387 the fault geometry from waveform inversion and seismicity alignment. The static moment
388 ($M_w 5.95$) also agrees well with the seismological moment ($M_w 6.0$). The slip distribution
389 shows an elongated rectangle shape that extends ~ 12 km along strike and ~ 5 km along dip,
390 centroid at a depth of 5 km, which is also very consistent with seismological results. Note
391 that although the centroid depth is very shallow, the slip did not reach to the surface, with
392 the top 3 km remaining un-ruptured. The along-strike length of slip distribution is fairly
393 consistent with the seismicity distribution.



394

395

396

397

Figure 7. Static slip model and InSAR data fitting. The top panel shows the slip model in depth and along dip profile. The InSAR data fitting for the ascending (upper) and descending (lower) tracks are showed in the lower panel.

398

399 4. Discussion

400

4.1 Unmapped active faults in the upper crust and interpretations

401

402

403

404

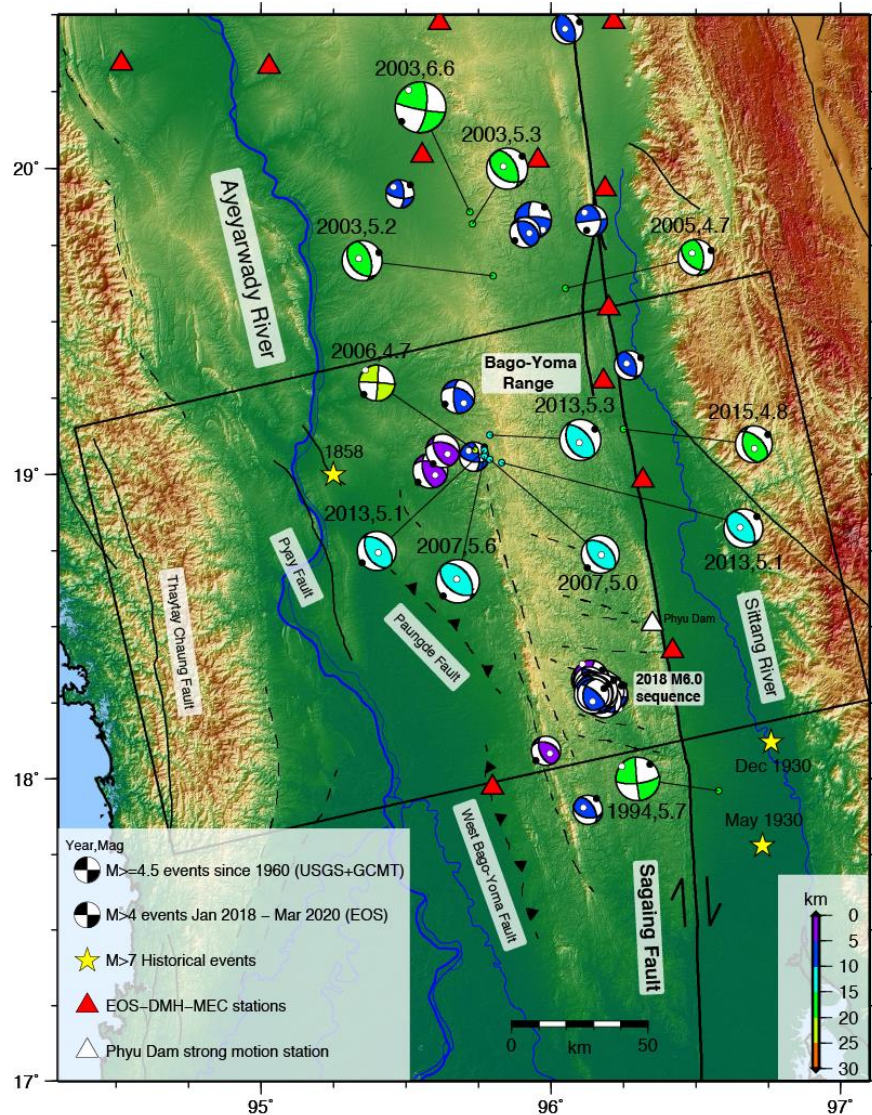
405

406

407

Although previous studies have mapped faults and lineaments oriented NW-SE and NNW-SSE in the BYR from satellite imagery, the sense of motion and slip rate of these faults have yet to be confirmed (Bender, 1983; Taylor & Yin, 2009; Wang et al., 2014; Rangin, 2017; Sloan et al., 2017). It is noteworthy that the ruptured fault of the 2018 sequence is not associated with any mapped active thrust faults that have been previously identified. Historical earthquakes in the region reported by global earthquake catalogs show that there has not been a $M > 4.5$ event within 30 km of the proposed

408 ruptured fault. However, there have been several $M > 4.5$ shallow thrust-faulting events
409 located to the northwest of the recent M_w 6.0 earthquake, with similar focal mechanisms,
410 such as the events in 2003, 2007 and 2013 (Fig. 8). In addition, we conducted focal
411 mechanism inversions for several $M > 4$ events in other regions along the western BYR
412 outside of the 2018 M_w 6.0 aftershock region (beachballs without year label in Fig. 8).
413 Intriguingly, these shallow events also show thrust-faulting focal mechanisms similar to
414 that of the 2018 event (Fig. 8). Note that the GCMT/USGS solutions in general have
415 greater depth (15-20 km) than our solutions (~5km). This is due to the lower depth
416 resolution in these global earthquake catalogs since they either use very long period for
417 waveform inversion or did not have nearby stations to suppress the origin time-depth
418 tradeoff. The P-axis direction from both strike-slip and thrust events all show an
419 orientation of NE-SW, which is consistent with the plate convergence direction of the
420 Indian plate relative to the Burma plate. In any case, these events are also not associated
421 with any mapped active faults. The shallow crustal events in this region occurring on
422 previously unidentified crustal structures may indicate that the very shallow part (a few
423 km) of the upper crust of the Burma Plate is actively deforming, and possibly
424 accommodating the distributed stresses due to the oblique subduction of the Indian plate
425 beneath the Burma Plate off the west coast of Myanmar (Fig. 1).



426

427

428

429

430

431

432

433

434

435

436

437

438

439

Figure 8. Crustal seismicity in the Bago-Yoma Range. $M > 4$ earthquakes (< 30 km deep) within and surrounding the Bago-Yoma Range from global earthquake catalogs (focal mechanisms with year and magnitude labeled) and our inversion of events recorded by the EOS-DMH-MEC stations (Jan 2018 – Mar 2020). We observe a trend of NW-SE striking thrust/oblique events along the BYR with occasional NS-EW striking strike-slip events.

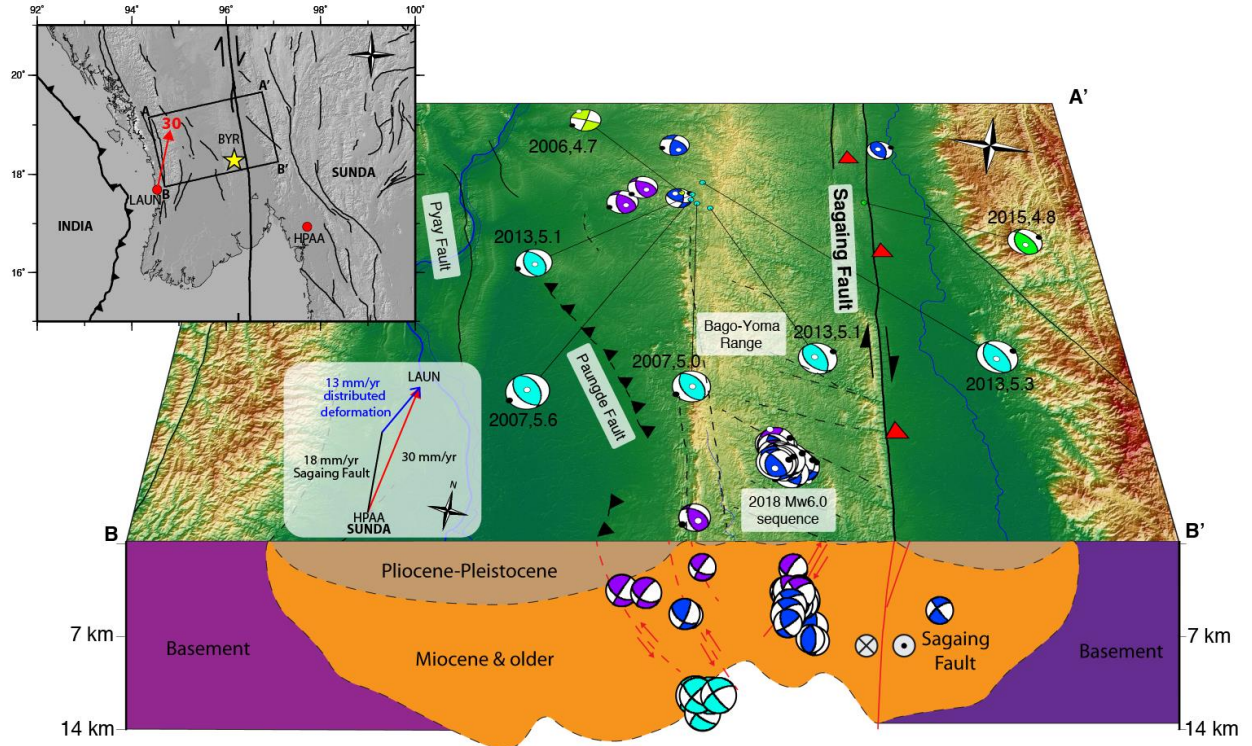
Previous publications have offered various hypotheses to explain the tectonic history of the Central Myanmar Basin (CMB) and southern Myanmar, within which the 2018 sequence occurred. Pivnik et al. (1998) used petroleum exploration data to show that the Salin sub-basin is a synclorium containing anticlines associated with the late-Miocene inversion structures, thrust sheets and low-relief uplifts. Bertrand and Rangin (2003) proposed that a regional plate kinematic reorganization occurred during the

440 Miocene which served as a transition between the transtensional tectonic regime related
441 to the opening of the CMB and the transpressional tectonic regime related to the
442 inversion of the CMB. Along the eastern CMB, Naing Maw Than et al. (2017) suggested
443 that the area underwent two tectonic phases; a compressional phase during the late
444 Miocene that formed the anticlines and synclines in the Pegu formations, followed by
445 strike-slip movement along the Sagaing Fault that resulted in an echelon faulting. In
446 general, most authors agree that the inner Burma plate has been subjected to
447 approximately E-W compression since the late-Miocene, which formed the structures
448 observed in and around the CMB. We observe that the P-axes of the thrust and strike-slip
449 events (Fig. 8 and 9) are in agreement with such compressional background stress in the
450 crust. Previous GPS observations also provide insights into the nature of deformation
451 west of the Sagaing Fault. Socquet et al. (2006) reveals that the Sagaing Fault only
452 absorbs a portion of the deformation between the western coast and Shan Plateau at the
453 latitude of 2018 earthquake (Fig.9 inset). The remaining deformation is primarily
454 distributed between the Sagaing Fault and the western coast at a rate of ~13mm/year in
455 the NNE direction, within which the BYR is located (Fig. 9, blue vector). We believe that
456 the 2018 Mw 6.0 earthquake is a result of the NE-SW shortening being accommodated
457 by a shallow thrust fault within the BYR, while the remaining deformation should be
458 distributed on other secondary faults, such as the West Bago Yoma Fault, Paungde Fault
459 and other unmapped faults, although the slip-rate of these faults are not yet known. To
460 further understand the geodynamics and geologic history of this oblique subduction zone
461 system, it is crucial to integrate geodetic and geologic observations along with detailed
462 and robust earthquake source parameters as presented here to produce a more
463 comprehensive and in-depth picture of the neotectonics.

464 Although there have been extensive oil and gas exploration efforts in the Central
465 Myanmar Basin, there is a lack of published seismic reflection data in the BYR region
466 due to the low hydrocarbon potential as indicated by surface geology (Ridd & Racey,
467 2015). Therefore, we are unable to compare our inferred thrust fault to structural maps or
468 seismic-reflection data in the southern BYR area. However, we can place our interpreted
469 fault geometry in a larger tectonic context of the Central Myanmar Basin by comparison
470 with the structural maps and seismic lines available further to the north and south of the
471 BYR (e.g., Pivnik et al., 1998; Ridd & Racey, 2015). Geologic cross-sections at latitudes
472 of ~20°-21°N show that both east- and west-dipping thrusts occur in this region, produced
473 by the inversion of the normal faults in the Salin synclinorium (see Fig. 2 in Pivnik et al.,
474 1998). Some of these thrusts truncate the Plio-Pleistocene Irrawaddy formation, and their
475 structural styles can be interpreted as positive flower structures. Their seismic profiles
476 also reveal anticlines to the west of BYR. Geologic cross-sections at latitudes of ~16.5°-
477 17.5°N also show both a large (~50km) and small (~10km) anticlines at ~50km to the
478 south of recent earthquake (see Fig. 4.23, 4.24 in Ridd & Racey, 2015). Since double-
479 vergence faults are common features found in many inverted sediment basins (e.g.,
480 Shinn, 2015; Pace & Calamita, 2014), and geological profiles north and south of our
481 study area both shows east- and west-dipping faults with regional late-Miocene basin
482 inversion history, we therefore suggest the fault that ruptured during the Mw 6.0 Bago-
483 Yoma earthquake is also associated with a pre-existing southwest-dipping fault within the
484 CMB area (Fig. 9). As the hypocenters of the Mw 6.0 earthquake sequence are limited at
485 a shallow depth range of 2 to 7 km, and previous studies suggest that the main fault

486 system at the western flank of BYR dips to the northeast (e.g. Wang et al., 2014), we
 487 further suggest that the ruptured southwest-dipping fault serves as the secondary fault in
 488 the push-up structure, and links to the main east-dipping fault at depth.

489 Unlike the thrust-type aftershocks, the source of the strike-slip aftershocks is less
 490 clear under the regional geological context. The four strike-slip aftershocks not only
 491 occurred in the footwall of the rupture fault, but also with fault orientation almost normal
 492 to the strike of the Sagaing Fault and other regional structures. As shown in geological
 493 maps of the BYR region (Naing Maw Than et al., 2017), and subsurface data of CMB
 494 area from Pivnik et al. (1998), the primary structures with both areas are intercepted by a
 495 series of shorter faults with E-W orientations. These cross faults within the BYR and
 496 CMB area may act as the conjugate faults co-developed with the primary inversion
 497 structures since the beginning of the oblique plate convergence. Although these structures
 498 are relatively minor, the stress-change from the Mw 6.0 mainshock may trigger the slip of
 499 the nearby cross faults and produce these deeper strike-slip aftershocks.



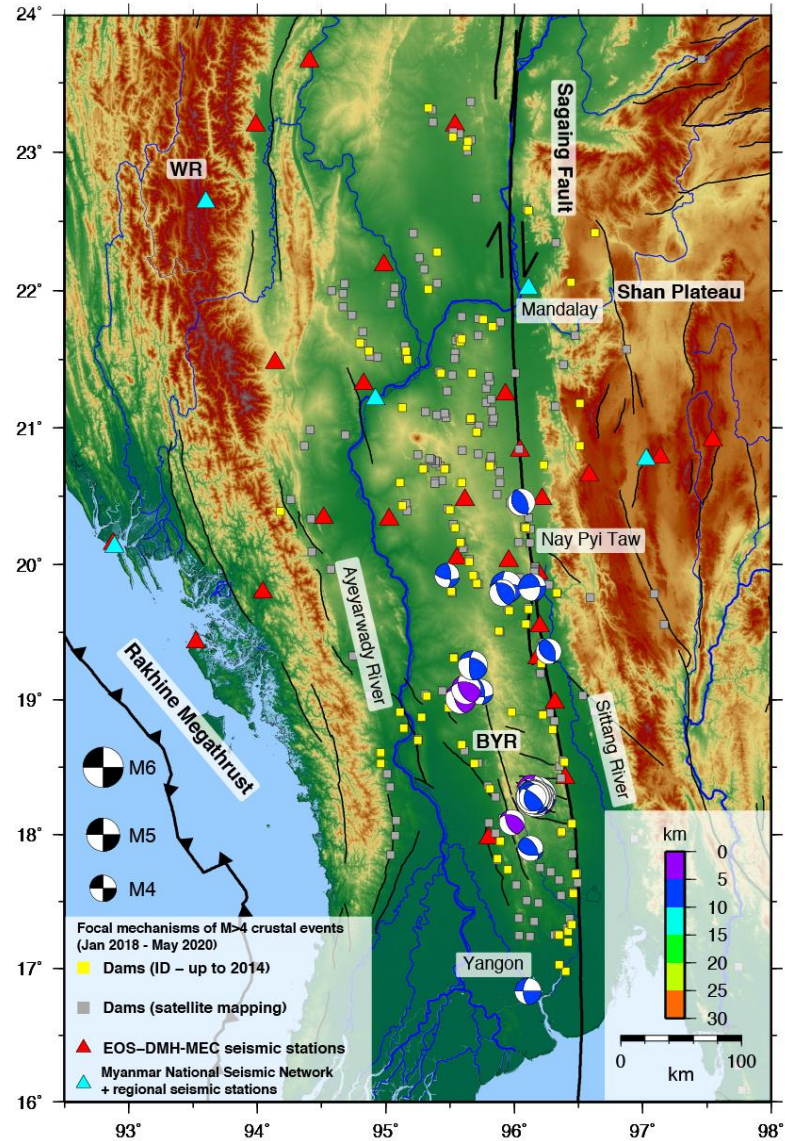
500

501 **Figure 9. Interpretation of deformation within the Bago-Yoma Range.** Schematic
 502 profile of the region at the location of the Mw6.0 earthquake sequence, modified from
 503 Ridd & Racey, 2015. (Inset) GPS velocity vector of LAUN with respect to HPAA/Sunda
 504 (red vector) and velocity diagram showing distributed deformation across southern
 505 Myanmar (blue vector), modified from Socquet et al., 2006.

506

507 4.2 Dams and seismic hazard

508 Due to its rugged topography, the BYR is sparsely populated and remains as a
509 dense forested area. Therefore, it serves as a rainwater-catchment area with channels
510 feeding into the southward flowing Ayeyarwady River to the west and the Sittang River
511 to the east (Fig. 10). There are numerous dams within the BYR, located along the
512 Sagaing Fault and along the eastern edge of the Western Range (Fig. 10). In the vicinity
513 of the 2018 Mw6.0 earthquake, there are several major dams ~25-35 km to the north (e.g.
514 Kun Dam, Phyu Chaung Dam) and south (e.g. Ye Nwe Dam, Baing Dar Dam). As
515 Myanmar becomes more developed, there is an increasing demand on hydropower and
516 irrigation from the dams. The spatial proximity of the dams to active faults, both mapped
517 and unmapped, represents an increased exposure to seismic hazard. When the source is
518 sufficiently shallow and close, even events as small as M4 can produce large Peak
519 Ground Acceleration (PGA) (e.g. Wei et al., 2015). Some cracks were detected on the
520 downstream side of the dam body of the South Nawin Dam after two shallow M>4
521 earthquakes occurred at the western edge of the BYR in October 2018 and followed by
522 smaller earthquakes until January 2019 (Tint Lwin Swe, 2019). The 2018 Mw 6.0 event
523 did not cause damage to the nearby dams, possibly because the closest dam was more
524 than 30 km away from the earthquake. In addition to damage due to natural earthquakes,
525 large reservoirs with significant impounding capacity can also trigger seismicity on
526 nearby faults, given favorable existing stress, permeability and pore fluid conditions
527 (Talwani & Acree, 1984; ICOLD, 2011; Ellsworth, 2013; Foulger et al., 2018).
528 Therefore, proximity to active faults and earthquake-resistant dam design are key factors
529 in planning and construction of dams in the region. We therefore further discuss the
530 attenuation of the ground motion produced by the 2018 Mw6.0 sequence.



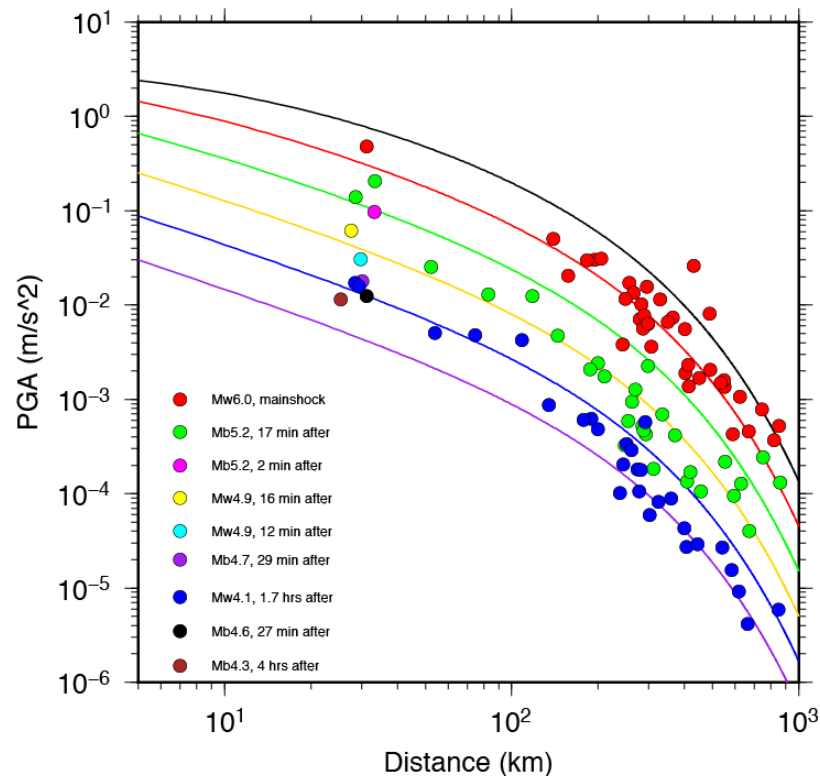
531

532 **Figure 10. Distribution of dams and active crustal faults in Myanmar.** Plot of focal
 533 mechanisms of M>4 crustal (<30 km deep) earthquakes from global earthquake catalogs
 534 and our inversion of events recorded by the EOS-DMH-MEC seismic stations. Dam
 535 locations provided from the Irrigation Department (ID) complete up to 2014 is indicated
 536 by the yellow squares while dam locations recently mapped from satellite imagery is
 537 indicated by gray squares. Active crustal seismicity within the BYR and along the
 538 Sagaing Fault, in close proximity to dams, suggest an increased seismic hazard to the
 539 population.

540

541 We plotted the PGA data for the mainshock (Mw6.0) and two early aftershocks
 542 (Mb5.2, Mw4.1) (Fig. 11), recorded by the broadband network and one strong motion
 543 station located at Phyu Dam, approximately 32 km away (white triangle in Fig. 8). We
 544 also plotted the PGA for several same-day M>4.3 aftershocks recorded by the strong

545 motion seismometer. Since there is no Ground Motion Prediction Equation (GMPE)
 546 available in the region, we adopted the hard rock GMPE in Japan (Zhao et al., 2006) for
 547 comparison and discussion. As the mainshock waveforms were clipped at the nearest
 548 broadband stations, the strong motion station provides valuable nearfield data in
 549 assessing the performance of the GMPE. In general, we find that the GMPE can fit the
 550 mainshock PGAs quite well, but does poorly for the smaller aftershocks, especially at
 551 distances larger than 50 km. Since the site classifications are not yet available for these
 552 sites, we did not take them into account in the attenuation analysis, which would be a
 553 major cause of the scattering and deviations in Fig. 11. This is left for future efforts,
 554 which are critical for the seismic hazard assessment in Myanmar.



555

556 **Figure 11. PGA analysis of the Mw6.0 Bago-Yoma earthquake sequence.** Colored
 557 circles represent PGA observed at the Phyu Dam strong motion station and EOS-DMH-
 558 MEC broadband stations. The location of Phyu Dam is indicated by a white triangle in
 559 Figure 8. Colored lines represent the calculated PGA from the GMPE proposed by Zhao
 560 et al. (2006). The PGA for the Mw6.0 sequence is consistent with the GMPE, but
 561 deviates from the GMPE as the magnitude decreases.

562

563 4.3 Complicated structure underneath Myanmar

564 The seismic record of the mainshock shows complicated waveforms recorded at
 565 the seismic stations throughout Myanmar (Fig. S6). The Pnl segment shows multiple
 566 arrivals possibly from a mix of reflected and depth phases, making it difficult to

567 determine the depth phases for constraining the focal depth (Fig 5b). The surface wave
568 segment shows a relatively large amplitude coda that extends for tens of seconds for
569 stations located on hard rock and longer for stations located within the Central Myanmar
570 Basin (Fig. S6), as also revealed by a previous study (Wang et al., 2019). Therefore, a 1D
571 velocity model is not able to adequately model the waveforms recorded at these stations
572 at sufficiently high frequencies to replicate the complicated Pnl arrivals. However, the
573 observed waveforms themselves provide several hints about the earthquake source. The
574 long duration coda of the surface waves supports our shallow focal depth results, since
575 earthquakes that nucleate at shallow depths are better able to produce high-amplitude and
576 long-duration surface wave coda compared to those that nucleate at deeper depths.
577 Aftershocks with thrust-faulting focal mechanisms located within ~2.5 km of each other
578 along the A-A' profile have similar waveforms as indicated by the high cross-correlation
579 coefficient values (Fig 5b), thus, validating our focal mechanism inversion results and
580 allow us to identify the moveout of possible depth phases. In addition, the observed
581 surface-/Pnl-wave amplitude ratios between these events allow us to infer the relative
582 depth of each event and support our depth inversion results that suggest a shallow SW-
583 dipping fault. To model these broadband waveforms, better 2D or 3D velocity models are
584 required.

585

586 **5. Conclusions**

587 We propose a fault geometry of (strike = 130° , dip = 40°) for the shallow thrust fault that
588 ruptured during the 11th January 2018, Mw 6.0 Bago-Yoma earthquake in southern Myanmar.
589 From high-resolution earthquake relocation and source parameter inversions, we infer that the
590 mainshock ruptured the fault ~10km along strike, with thrusting aftershocks located at depths
591 between 3-7 km. We also find that the mainshock triggered deeper (7-8 km) strike-slip
592 aftershocks a few km to the east of the mainshock epicenter. Combined with InSAR
593 observations, static slip inversion, depth-phase analysis, historical seismicity, and previous
594 geologic studies, the results and observations support a thrust fault dipping to the SW at an angle
595 of approximately 40° , which we interpret to be a pre-existing fault within the BYR anticlinorium.
596 Our findings highlight the complexity of the tectonics of southern Myanmar, where this
597 earthquake sequence and several other $M > 4$ crustal earthquakes in the region indicate ongoing
598 distributed deformation between the oblique Rakhine megathrust and the dextral Sagaing Fault.
599 With the development of more infrastructure such as dams within and surrounding the BYR,
600 more high-resolution seismological studies on existing faults and potentially active intraplate
601 faults and their associated hazards must be conducted.

602

603 **Acknowledgments**

604 This research is supported by the National Research Foundation Singapore and the Singapore
605 Ministry of Education under the Research Centers of Excellence initiative via the Earth
606 Observatory of Singapore (EOS) grant 04MNS001848A620. The EOS-DMH-MEC seismic data
607 was accessed from the EOS Center for Geohazard Observation (CGO); we thank the CGO for

608 installing and servicing the EOS-DMH-MEC seismic array. We are grateful to the Department of
 609 Meteorology and Hydrology of Myanmar and Myanmar Earthquake Committee for their help in
 610 installing the EOS-DMH-MEC seismic array. The EOS-DMH-MEC seismic waveform data used
 611 in this study can be accessed from (<https://doi.org/10.21979/N9/BQ11DP>) and the ALOS-2
 612 InSAR data used in the static slip inversion can be accessed from
 613 (<https://doi.org/10.21979/N9/QHJXU7>). Seismic data from the MM and TM network were
 614 downloaded through the Incorporated Research Institutions for Seismology (IRIS) website
 615 (<https://www.iris.edu/hq/>). ALOS-2 SAR data were obtained from the Japanese Aerospace
 616 Agency (JAXA) under RA-6 project number 3240 awarded to E. Lindsey. Mapping of dams
 617 from satellite imagery was conducted using Google Earth. Sac 2000, Taup (Crotwell et al.,
 618 1999), and GMT (Wessel et al., 2013) were used for basic data processing and figure
 619 development. We are grateful to Kyle Bradley for useful discussions.

620

621 **References**

- 622 Bertrand, G., & Rangin, C. (2003). Tectonics of the western margin of the Shan plateau (central
 623 Myanmar): Implication for the India-Indochin oblique convergence since the Oligocene. *Journal*
 624 *of Asian Earth Sciences*, 21(10), 1139–1157. [https://doi.org/10.1016/S1367-9120\(02\)00183-9](https://doi.org/10.1016/S1367-9120(02)00183-9).
- 625 Bender, F., and D. N. Bannert (1983), *Geology of Burma*, Science Publishers, Gebruder
 626 Borntraeger Verlagsbuchhandlung.
- 627 Chen, C. W., & Zebker, H. A. (2000). Network approaches to two-dimensional phase
 628 unwrapping: intractability and two new algorithms: erratum. *Journal of the Optical Society of*
 629 *America A*, 17(3), 401–414. <https://doi.org/10.1364/josaa.18.001192>.
- 630 Chen, W., & Molnar, P. (1990). Source parameters of earthquakes and intraplate deformation
 631 beneath the Shillong Plateau and Northern Indo-Burman Ranges. *Journal of Geophysical*
 632 *Research*, 95(90), 12527–12552. <https://doi.org/10.1029/JB095iB08p12527>.
- 633 Chhibber, H. L., and R. Ramamirtham (1934), *The geology of Burma*, MacMillan, London, U.
 634 K.
- 635 Chit Tet Mon, Gong, X., Wen, Y., Jiang, M., & Chen, Q. F. (2020). Insight Into Major Active
 636 Faults in Central Myanmar and the Related Geodynamic Sources, *Geophysical Research Letters*,
 637 47, 1–8. <https://doi.org/10.1029/2019GL086236>.
- 638 DeMets, C., Gordon, R. G., & Argus, D. F. (2010). Geologically current plate motions.
 639 *Geophysical Journal International*, 181(1), 1–80. [https://doi.org/10.1111/j.1365-](https://doi.org/10.1111/j.1365-246X.2009.04491.x)
 640 [246X.2009.04491.x](https://doi.org/10.1111/j.1365-246X.2009.04491.x).
- 641 Dziewonski, A. M., Chou, T. A., & Woodhouse, J. H. (1981). Determination of earthquake
 642 source parameters from waveform data for studies of global and regional seismicity. *Journal of*
 643 *Geophysical Research*, 86(B4), 2825–2852. <https://doi.org/10.1029/JB086iB04p02825>.
- 644 Ekström, G., Nettles, M., & Dziewoński, A. M. (2012). The global CMT project 2004-2010:
 645 Centroid-moment tensors for 13,017 earthquakes. *Physics of the Earth and Planetary Interiors*,
 646 200–201, 1–9. <https://doi.org/10.1016/j.pepi.2012.04.002>
- 647 Ellsworth, W. L. (2013). Injection-Induced Earthquakes. *Science*, 341, 1–8.
 648 <https://doi.org/10.1126/science.1225942>.

- 649 Foulger, G. R., Wilson, M. P., Gluyas, J. G., Julian, B. R., & Davies, R. J. (2018). Global review
650 of human-induced earthquakes. *Earth-Science Reviews*, 178(July 2017), 438–514.
651 <https://doi.org/10.1016/j.earscirev.2017.07.008>.
- 652 Hrin Nei Thiam, Htwe, Y. M. M., Kyaw, T. L., Tun, P. P., Min, Z., Htwe, S. H., ... Hough, S. E.
653 (2017). A report on upgraded seismic monitoring stations in Myanmar: Station performance and
654 site response. *Seismological Research Letters*, 88(3), 926–934.
655 <https://doi.org/10.1785/0220160168>.
- 656 Hurukawa, N., & Maung Maung, P. (2011). Two seismic gaps on the Sagaing Fault, Myanmar,
657 derived from relocation of historical earthquakes since 1918. *Geophysical Research Letters*,
658 38(1), 1–5. <https://doi.org/10.1016/j.earscirev.2017.07.008>.
- 659 ICOLD (International Commission on Large Dams) (2011). Reservoir and Seismicity: State of
660 Knowledge. *International Commission on Large Dams Bulletin 137*, p. 1-110.
- 661 Jónsson, S., Zebker, H., Segall, P., & Amelung, F. (2002). Earthquake, Estimated from Satellite
662 Radar and GPS Measurements. *Bulletin of the Seismological Society of America*, 92(4), 1377-
663 1389. <https://doi.org/10.1785/0120000922>.
- 664 Laske, G., Masters., G., Ma, Z. and Pasyanos, M. (2013). Update on CRUST1.0 - A 1-degree
665 Global Model of Earth's Crust, *Geophys. Res. Abstracts*, 15, Abstract EGU2013-2658.
- 666 Le Dain, A. Y., Tapponnier, P., & Molnar, P. (1984). Active Faulting and Tectonics of Burma
667 and Surrounding Regions. *Journal of Geophysical Research*, 89(B1), 453–472.
668 <https://doi.org/10.1029/JB089iB01p00453>.
- 669 Mallick, R., Lindsey, E. O., Feng, L., Hubbard, J., Banerjee, P., & Hill, E. M. (2019). Active
670 Convergence of the India-Burma-Sunda Plates Revealed by a New Continuous GPS Network.
671 *Journal of Geophysical Research: Solid Earth*, 124(3), 3155–3171.
672 <https://doi.org/10.1029/2018JB016480>.
- 673 Maung Thein, Than Myint, Soe Thura Tun & Tint Lwin Swe (2009). Earthquake and tsunami
674 hazard in Myanmar. *Journal of Earthquake and Tsunami*, 3(2), 43–57.
675 <https://doi.org/10.1142/S1793431109000482>.
- 676 Naing Maw Than, Khin, K., & Thein, M. (2017). Chapter 7: Cretaceous geology of Myanmar
677 and Cenozoic geology in the Central Myanmar Basin. *Geological Society, London, Memoirs*,
678 48(1), 143–167. <https://doi.org/10.1144/m48.7>.
- 679 NASA JPL (2013). NASA Shuttle Radar Topography Mission Global 1 arc second, distributed
680 by NASA EOSDIS Land Processes DAAC,
681 <https://doi.org/10.5067/MEaSURES/SRTM/SRTMGL1.003>.
- 682 Ni, J. F., Guzman-Speziale, M., Bevis, M., Holt, W. E., Wallace, T. C., & Seager, W. R. (1989).
683 Accretionary tectonics of Burma and the three-dimensional geometry of the Burma subduction
684 zone. *Geology*, 17(1), 68–71. [https://doi.org/10.1130/0091-7613\(1989\)017<0068:ATOBAT>2.3.CO;2](https://doi.org/10.1130/0091-7613(1989)017<0068:ATOBAT>2.3.CO;2)
- 686 Oldham, T. (1883). A catalogue of Indian earthquakes from the earliest time to the end of A.D.
687 1869, Memoir. Geol. Surv. India, 29, 163–215.

- 688 Pace, P., & Calamita, F. (2014). Push-up inversion structures v. fault-bend reactivation anticlines
689 along oblique thrust ramps: Examples from the Apennines fold-and-thrust belt (Italy). *Journal of*
690 *the Geological Society*, *171*(2), 227–238. <https://doi.org/10.1144/jgs2013-053>.
- 691 Pivnik, D. A., Nahm, J., Tucker, R. S., Smith, G. O., Nyein, K., Nyunt, M., & Maung, P. H.
692 (1998). Polyphase deformation in a fore-arc/back-arc basin, Salin subbasin, Myanmar (Burma).
693 *AAPG Bulletin*, *82*(10), 1837–1856. [https://doi.org/10.1306/1D9BD15F-172D-11D7-](https://doi.org/10.1306/1D9BD15F-172D-11D7-8645000102C1865D)
694 [8645000102C1865D](https://doi.org/10.1306/1D9BD15F-172D-11D7-8645000102C1865D).
- 695 Rangin, C. (2017). Chapter 3: Active and recent tectonics of the Burma Platelet in Myanmar.
696 *Geological Society, London, Memoirs*, *48*(1), 53–64. <https://doi.org/10.1144/M48.3>.
- 697 Ridd, M. F. & Racey, A. (2015). Chapter 4: Onshore petroleum geology of Myanmar : Central
698 Burma Depression. *Geological Society, London, Memoirs*, *45*(1), 21–50.
699 <https://doi.org/10.1144/M45.04>.
- 700 Sandwell, D., Mellors, R., Tong, X., Wei, M., & Wessel, P. (2011). Open radar interferometry
701 software for mapping surface deformation. *Eos, Transactions American Geophysical Union*,
702 *92*(28), 234-235. <https://doi.org/10.1029/2011EO280002>.
- 703 Shinn, Y. J. (2015). Geological structures and controls on half-graben inversion in the western
704 Gusan Basin, Yellow Sea. *Marine and Petroleum Geology*, *68*, 480–491.
705 <https://doi.org/10.1016/j.marpetgeo.2015.09.013>.
- 706 Shyu, J. B. H., Wang, C. C., Wang, Y., Shen, C. C., Chiang, H. W., Liu, S. C., ... Tun, S. T.
707 (2018). Upper-plate splay fault earthquakes along the Arakan subduction belt recorded by
708 uplifted coral microatolls on northern Ramree Island, western Myanmar (Burma). *Earth and*
709 *Planetary Science Letters*, *484*, 241–252. <https://doi.org/10.1002/jgrb.50121>.
- 710 Simons, M., Fialko, Y., & Rivera, L. (2002). Coseismic deformation from the 1999 Mw 7.1
711 Hector Mine, California, earthquake as inferred from InSAR and GPS observations. *Bulletin of*
712 *the Seismological Society of America*, *92*(4), 1390–1402. <https://doi.org/10.1785/0120000933>.
- 713 Sloan, R. A., Elliott, J. R., Searle, M. P., & Morley, C. K. (2017). Chapter 2: Active tectonics of
714 Myanmar and the Andaman Sea. *Geological Society, London, Memoirs*, *48*(1), 19–52.
715 <https://doi.org/10.1144/M48.2>.
- 716 Socquet, A., Vigny, C., Chamot-Rooke, N., Simons, W., Rangin, C., & Ambrosius, B. (2006).
717 India and Sunda plates motion and deformation along their boundary in Myanmar determined by
718 GPS. *Journal of Geophysical Research: Solid Earth*, *111*(5), 1–11.
719 <https://doi.org/10.1029/2005JB003877>.
- 720 Steckler, M. S., Akhter, S. H., & Seeber, L. (2008). Collision of the Ganges-Brahmaputra Delta
721 with the Burma Arc: Implications for earthquake hazard. *Earth and Planetary Science Letters*,
722 *273*(3–4), 367–378. <https://doi.org/10.1016/j.epsl.2008.07.009>.
- 723 Talwani, P., & Acree, S. (1984). Pore pressure diffusion and the mechanism of dams-induced
724 seismicity. *Pure and Applied Geophysics PAGEOPH*, *122*(6), 947–965. <https://doi.org/10.1007/BF00876395>.
- 726 Taylor, M., & Yin, A. (2009). Active structures of the Himalayan-Tibetan orogen and their
727 relationships to earthquake distribution, contemporary strain field, and Cenozoic volcanism.
728 *Geosphere*, *5*(3), 199–214. <https://doi.org/10.1130/GES00217.1>.

- 729 Tint Lwin Swe (2019). Importance of active tectonic studies of the Bago-Yoma anticlinorium for
730 major civil engineering projects [Abstract]. *7th International Workshop on Seismotectonics in*
731 *Myanmar and Earthquake Risk Management (SMERM 2019)*, 4-5.
- 732 Wang, Y., Shyu, J. B. H., Sieh, K., Chiang, H. W., Wang, C. C., Aung, T., ... Tun, S. T. (2013).
733 Permanent upper plate deformation in western Myanmar during the great 1762 earthquake:
734 Implications for neotectonic behavior of the northern Sunda megathrust. *Journal of Geophysical*
735 *Research: Solid Earth*, 118(3), 1277–1303. <https://doi.org/10.1002/jgrb.50121>.
- 736 Wang, Y., Sieh, K., Soe, T. T., Lai, K.-Y., & Myint, T. (2014). Active tectonics and earthquake
737 potential of the Myanmar region. *Journal of Geophysical Research: Solid Earth*, 3576–3822.
738 <https://doi.org/10.1002/2013JB010762>
- 739 Wang, X., Wei, S., Wang, Y., Maung Maung, P., Hubbard, J., Banerjee, P., ... Almeida, R.
740 (2019). A 3-D Shear Wave Velocity Model for Myanmar Region. *Journal of Geophysical*
741 *Research: Solid Earth*, 124, 1-23. <https://doi.org/10.1029/2018JB016622>
- 742 Wang, Y., Sieh, K., Aung, T., Min, S., Khaing, S. N., & Tun, S. T. (2011). Earthquakes and slip
743 rate of the southern Sagaing fault: Insights from an offset ancient fort wall, lower Burma
744 (Myanmar). *Geophysical Journal International*, 185(1), 49–64. [https://doi.org/10.1111/j.1365-](https://doi.org/10.1111/j.1365-246X.2010.04918.x)
745 [246X.2010.04918.x](https://doi.org/10.1111/j.1365-246X.2010.04918.x)
- 746 Wei, S., Avouac, J.P., Hudnut, K.W., Donnellan, A., Parker, J.W., Graves, R.W., Helmberger,
747 D., Fielding, E., Liu, Z., Cappa, F. and Eneva, M., 2015. The 2012 Brawley swarm triggered by
748 injection-induced aseismic slip. *Earth and Planetary Science Letters*, 422, pp.115-125.
749 <https://doi.org/10.1016/j.epsl.2015.03.054>
- 750 Zhao, J. X., Zhang, J., Asano, A., Ohno, Y., Oouchi, T., Takahashi, T., ... Fukushima, Y. (2006).
751 Attenuation relations of strong ground motion in Japan using site classification based on
752 predominant period. *Bulletin of the Seismological Society of America*, 96(3), 898–913.
753 <https://doi.org/10.1785/0120050122>
- 754 Zhu, L., & Ben-Zion, Y. (2013). Parametrization of general seismic potency and moment tensors
755 for source inversion of seismic waveform data. *Geophysical Journal International*, 194(2), 839–
756 843. <https://doi.org/10.1093/gji/ggt137>
- 757 Zhu, L., & Helmberger, D. V. (1996). Advancement in source estimation techniques using
758 broadband regional seismograms. *Bulletin of the Seismological Society of America*, 86(5), 1634–
759 1641. <https://doi.org/10.1785/0120160029>
- 760 Zhu, L., & Rivera, L. A. (2002). A note on the dynamic and static displacements from a point
761 source in multilayered media. *Geophysical Journal International*, 148, 619–627.
762 [https://doi.org/ https://doi.org/10.1046/j.1365-246X.2002.01610.x](https://doi.org/10.1046/j.1365-246X.2002.01610.x)

The 11th January 2018, Mw 6.0 Bago-Yoma, Myanmar earthquake: A shallow thrust event within the deforming Bago-Yoma Range**Wardah Fadil^{1,2}, Eric O. Lindsey¹, Yu Wang³, Phyo Maung Maung¹, Heng Luo⁴, Tint Lwin Swe⁵, Pa Pa Tun⁶, Shengji Wei^{1,2}**¹Earth Observatory of Singapore, Nanyang Technological University, Singapore²Asian School of the Environment, Nanyang Technological University, Singapore³National Taiwan University, Taiwan⁴State Key Laboratory of Information Engineering in Surveying, Mapping, and Remote Sensing, Wuhan University, China⁵Myanmar Earthquake Committee, Myanmar⁶Department of Meteorology and Hydrology, Myanmar**Contents of this file**

Figures S1 to S6

Introduction

This file includes the velocity model used in the earthquake relocation and CAP focal mechanism inversion, InSAR processing steps, the mainshock grid search results as an example for the earthquake epicenter relocation, complete CAP focal mechanism and depth inversion results for the mainshock and four aftershocks highlighted in the main text, static slip inversion results for the NE-dipping fault, and a record section of the mainshock waveforms for stations up to 300 km.

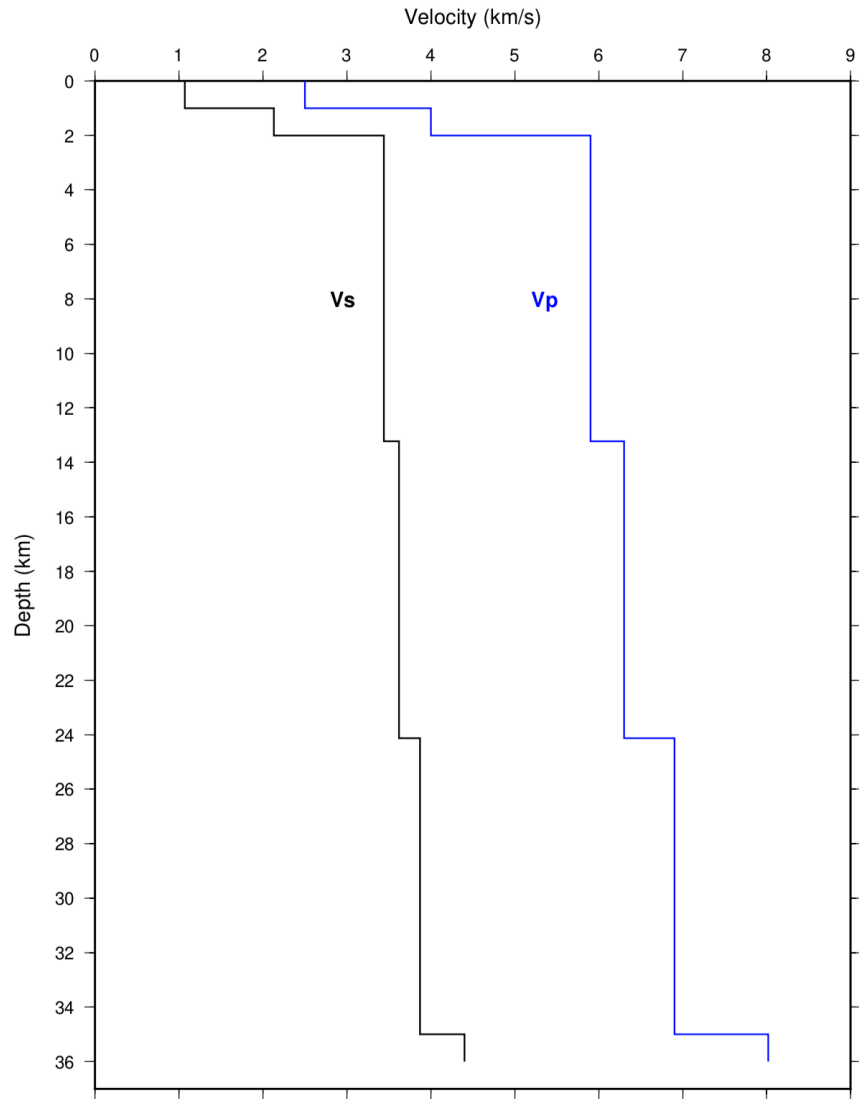


Figure S1. 1D velocity model from CRUST1.0 at the mainshock source location (18.5°N, 96.5°E).

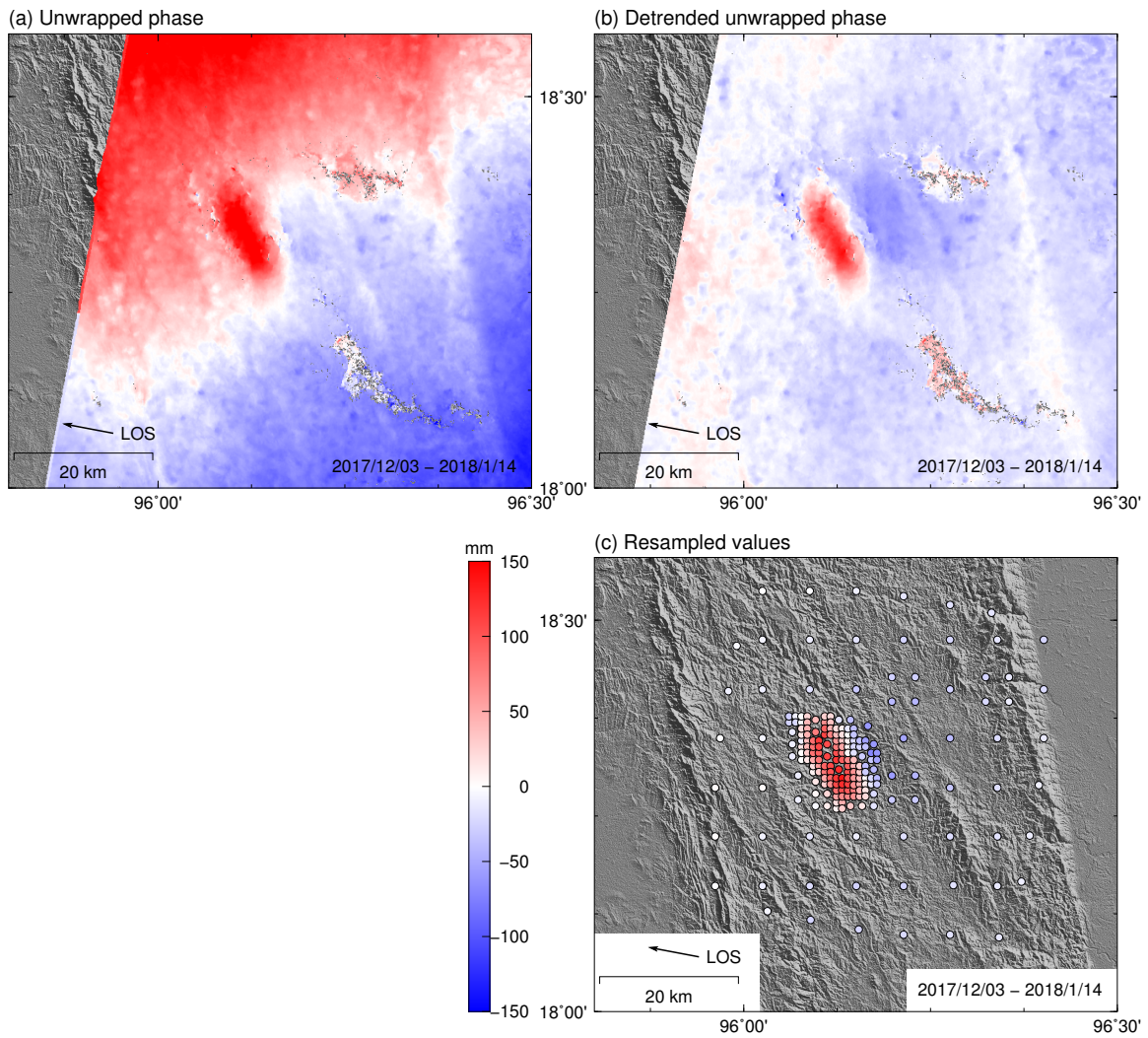


Figure S2. InSAR processing steps. (a) Filtered, unwrapped phase from ALOS-2 Path 41, Frame 3250, subswath 3. (b) Unwrapped phase after gaussian highpass filtering at 100 km wavelength and removing the topographically correlated atmospheric delay. (c) Unwrapped, detrended phase after quadtree resampling with a variance threshold of 12mm.

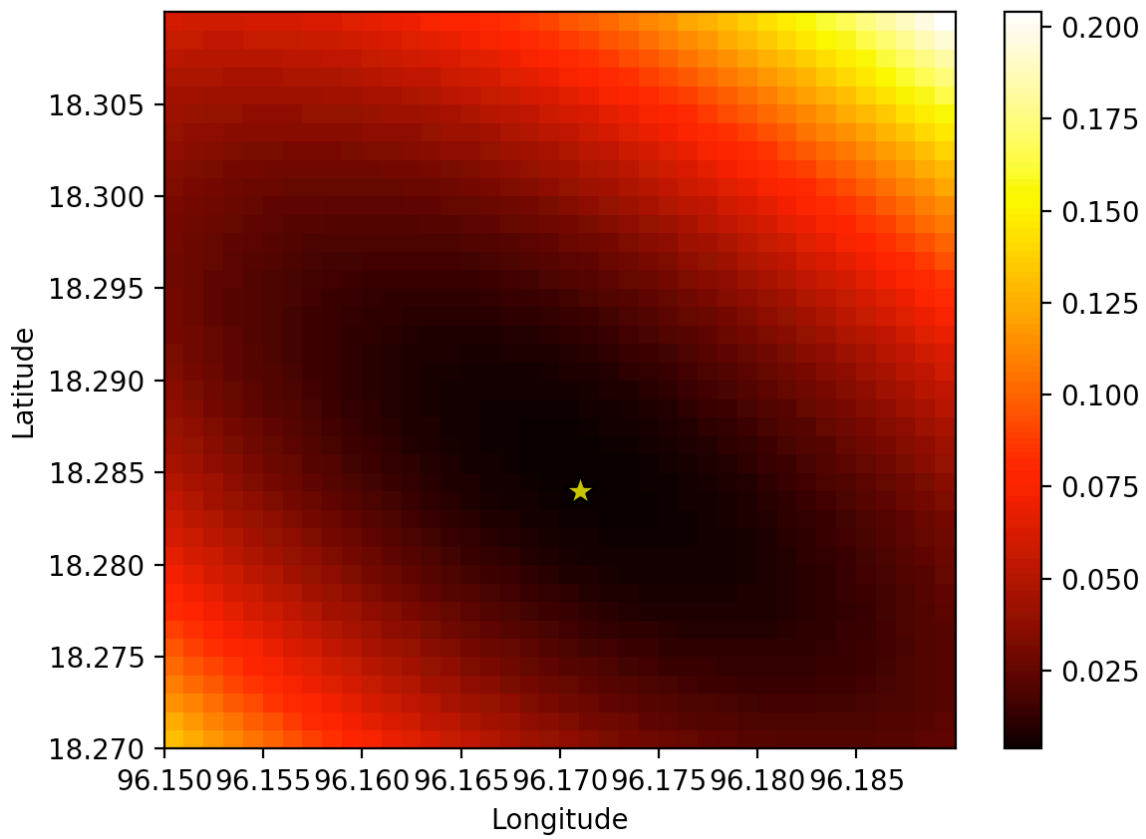


Figure S3. Plot of error values (L2-norm) within the grid search area. Yellow star shows best epicenter with minimum error. Error values indicate that the location uncertainty is largest in the NW-SE direction, due to the distribution of stations used in the grid search.

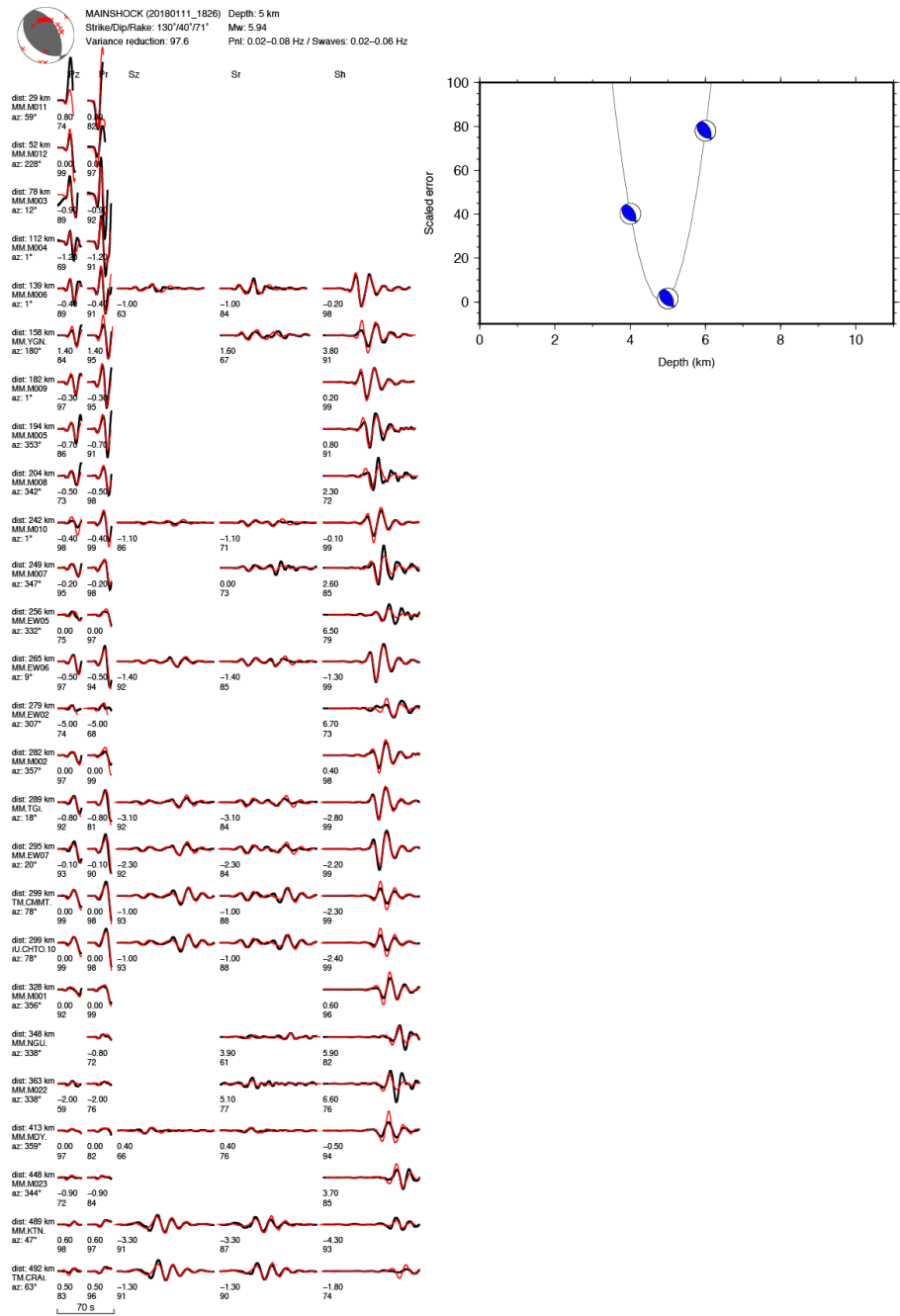


Figure S4(a). Focal mechanism inversion results (CAP) for the Mw 6.0 mainshock. (Left) Waveform fits between data (black) and synthetics (red) produced by the focal mechanism with minimum misfit (indicated in top left), at the stated frequency range for Pnl- and S-wave segments. Station name, distance and azimuth are indicated at the leftmost column of each station waveform, followed by the Pnl – Z component, Pnl – Radial component, S-waves – Z component, S-waves – Radial component, S-waves – Tangential component. The first number below each segment indicates the time shift (sec) followed by the waveform cross-correlation coefficient (%). (Right) Plot of errors for a range of focal depths normalized to the minimum error, showing the best depth at ~4.8 km.

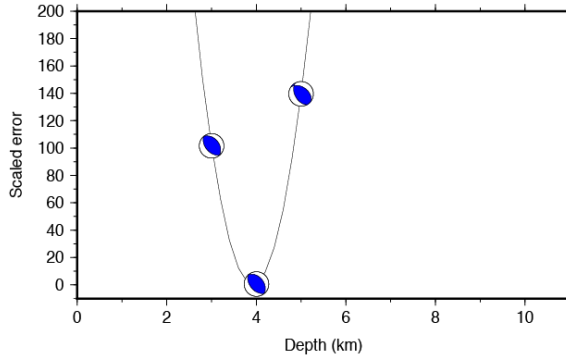
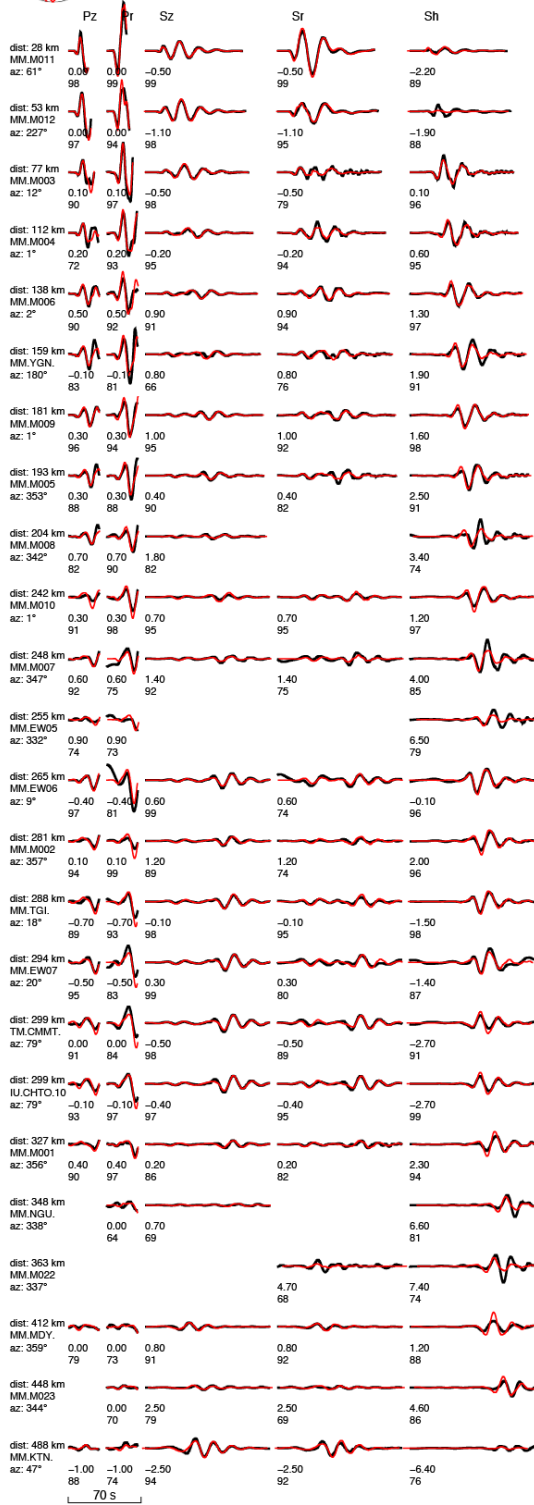
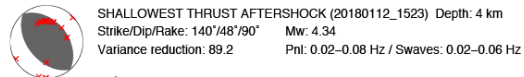


Figure S4(b). Focal mechanism inversion results (CAP) for shallowest thrust aftershock.

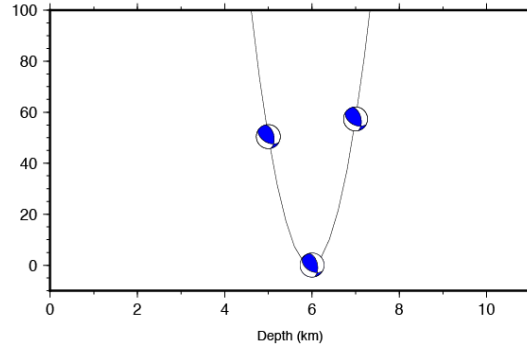
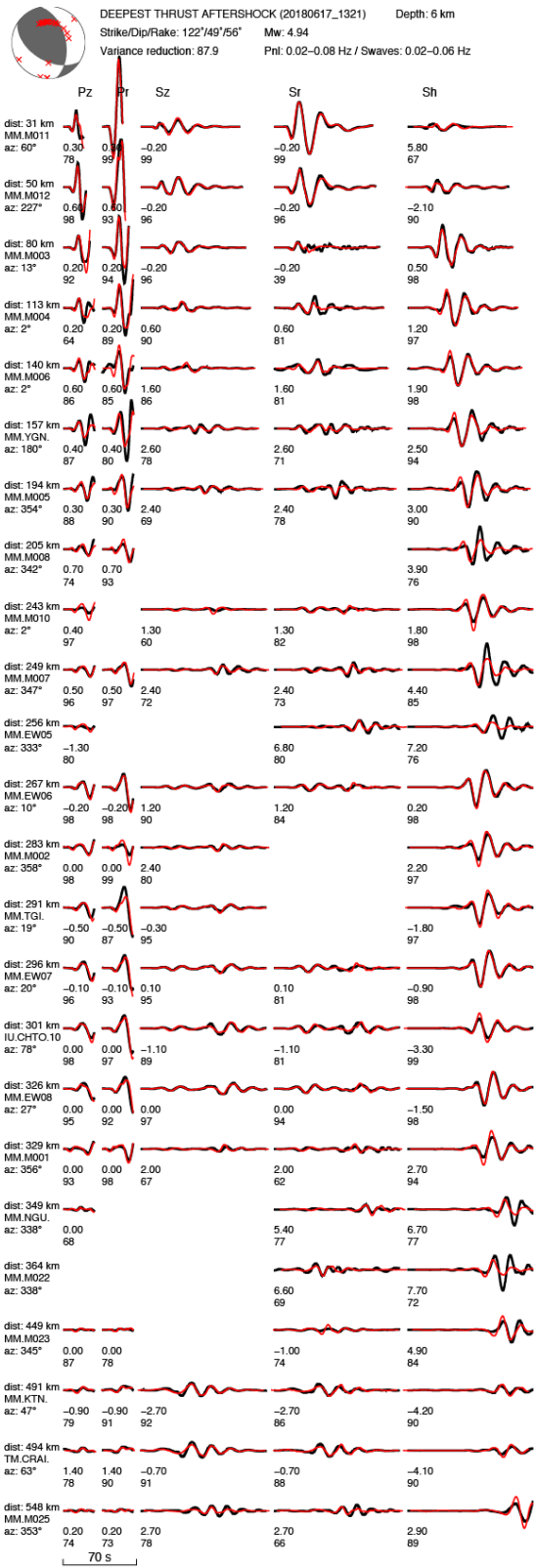


Figure S4(c). Focal mechanism inversion results (CAP) for deepest thrust aftershock.

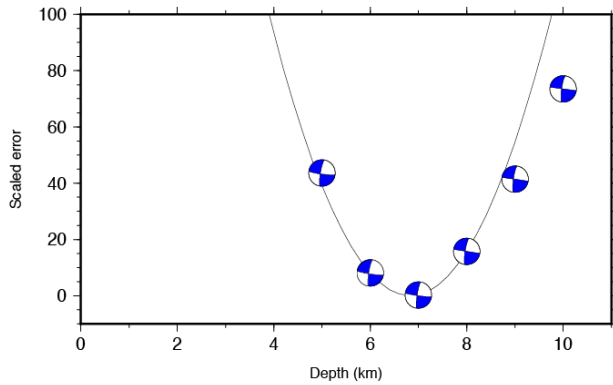
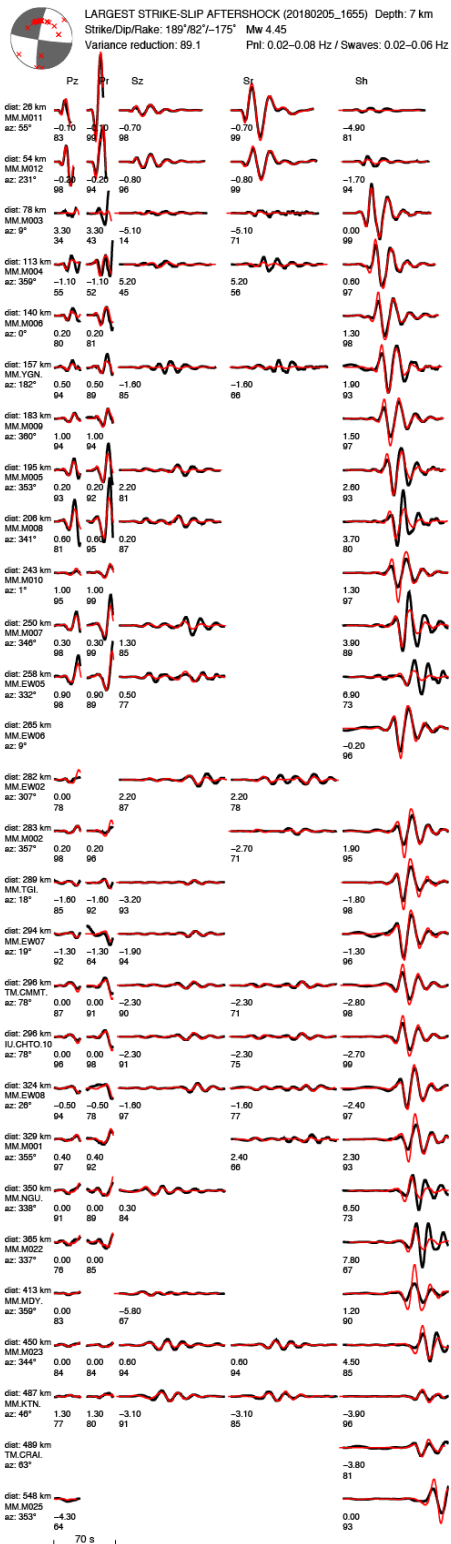


Figure S4(d). Focal mechanism inversion results (CAP) for the largest strike-slip aftershock.

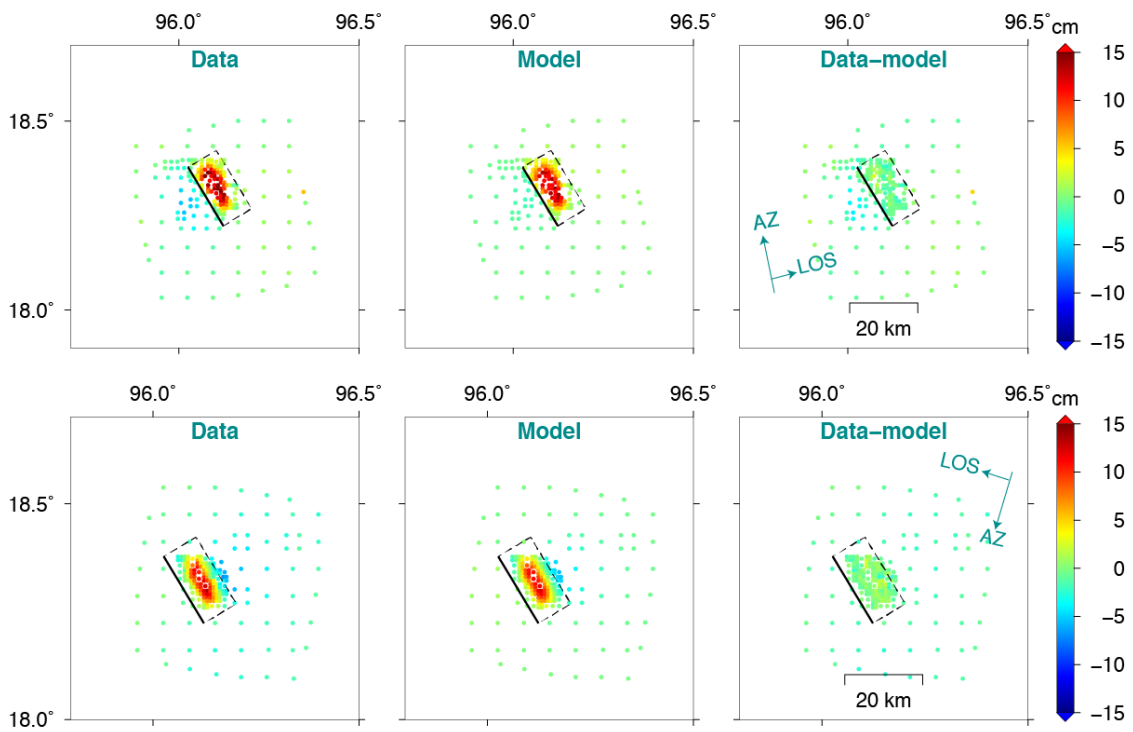
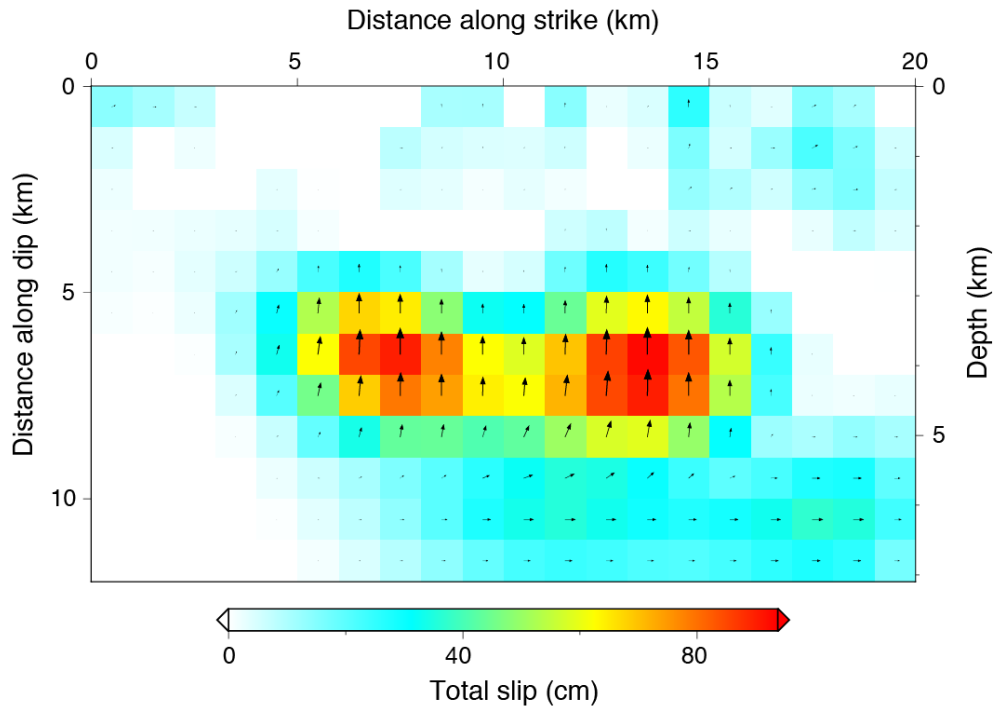


Figure S5. Static slip inversion results for northeast-dipping fault. The top panel shows the slip model in depth and along dip profile for the northeast-dipping fault. The InSAR data fitting for the ascending (upper) and descending (lower) tracks are showed in the lower panel.

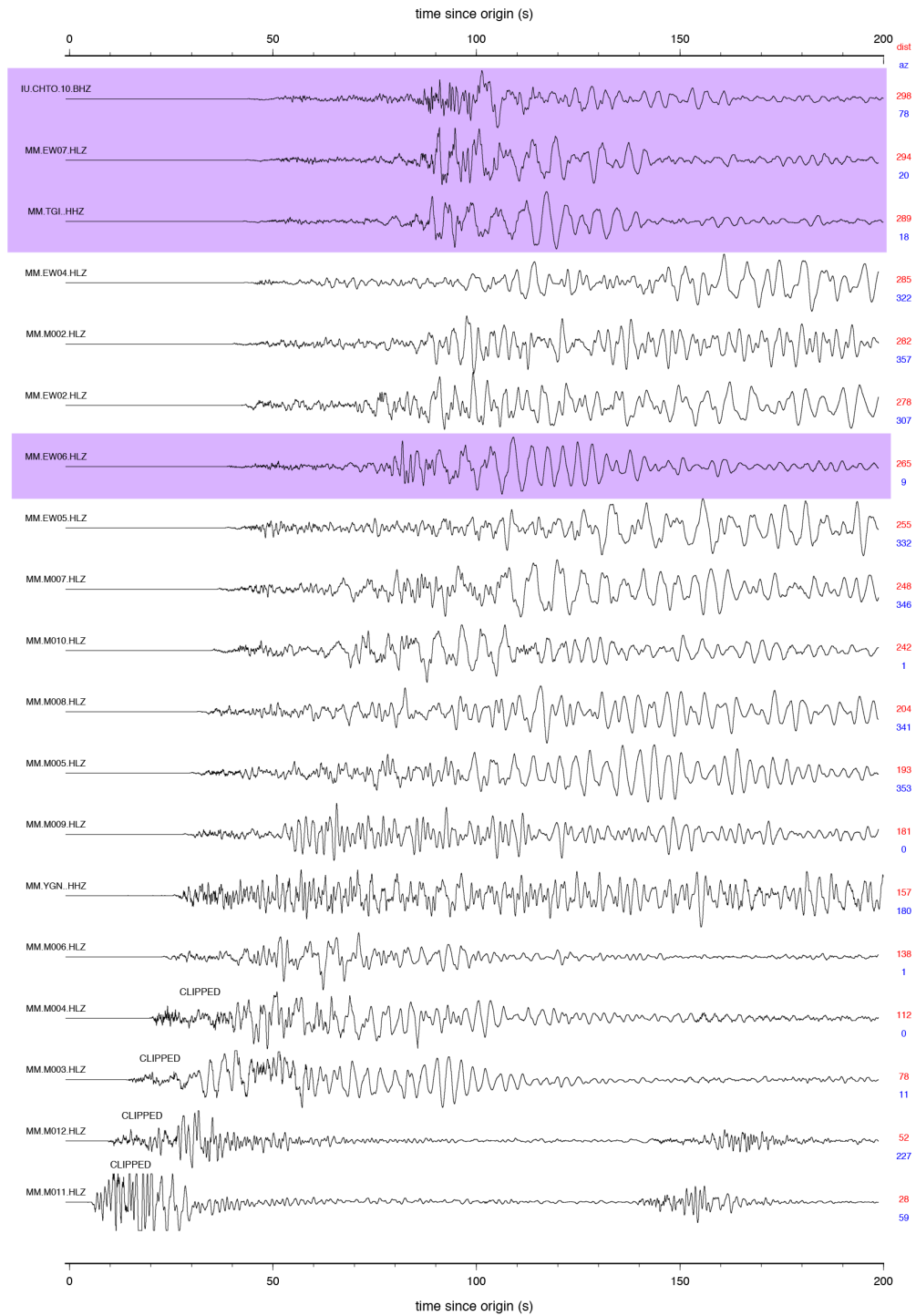


Figure S6. Record section of vertical component of the Mw6.0 mainshock recorded by the regional seismic stations, showing high amplitude and long-period surface wave coda. Waveforms highlighted in purple are recorded at hard rock stations. Distance (red) and azimuth (blue) are indicated for each station.